Utrecht University

Royal Netherlands Institute for Sea Research

Master Thesis
MSc. Climate Physics

THE IMPORTANCE OF REGIONAL OCEAN MODELLING FOR SEA-LEVEL PROJECTIONS IN THE NORTH-WEST EUROPEAN SHELF REGION

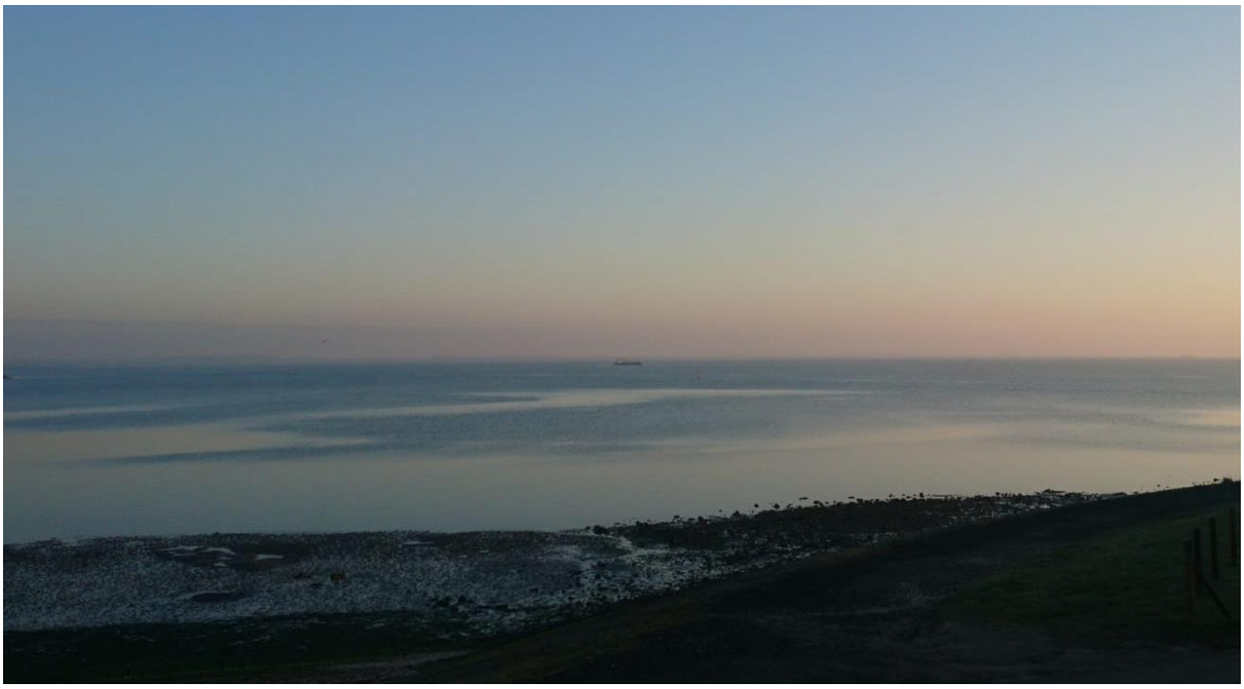

16-10-2020

Author:

Annette D. van den Engel
6370187

Supervisors:

Dr. Ir. A.B.A. (Aimée) Slangen (EDS)
Prof. Dr. R.S.W. (Roderik) van de Wal (IMAU)
Ir. T.H.J. (Tim) Hermans (EDS)
Dr. C.H. (Carleen) Tijm-Reijmer (IMAU)

This master thesis was performed at the Department of Estuarine & Delta Systems (EDS) of the Royal Institute for Sea Research (NIOZ) in collaboration with the Institute for Marine and Atmospheric research Utrecht (IMAU) of the Utrecht University (UU)

Abstract

Regional sea-level projections are of interest, because they can strongly deviate from the global mean sea-level change. In a previous study, dynamical downscaling was found to give more realistic simulations in the Northwestern European Shelf (NWES) region than coarse-resolution global climate models (GCMs) of the Coupled Model Intercomparison Project Phase 5 (CMIP5). Dynamical downscaling uses high-resolution regional climate models (RCMs) to refine the GCM results. Here we investigate the performance of dynamically downscaling sea-level projections in the NWES region with the regional ocean model (ROM) ROMS. The simulations are performed over the period from 1980 to 2098, on a 1/4° by 1/4° horizontal grid resolution. ROMS is forced at the lateral boundaries with the CMIP5 GCM HadGEM2-ES ocean component. The ROMS surface boundary is forced by the dynamically downscaled HadGEM2-ES atmosphere component with the regional atmosphere model (RAM) RCA4 from the EURO-CORDEX database. The downscaled sea-level projections are compared to the HadGEM2-ES data and the results from (Hermans, Tinker, et al., 2020), where HadGEM2-ES was dynamically downscaled with the ROM NEMO AMM7 (with a horizontal grid resolution of 1/15° by 1/9°).

We find that dynamical downscaling with ROMS leads to a reduced sea-level rise in the North Sea for the end of the twenty-first century compared to HadGEM2-ES (13 cm for the Belgian, Dutch and Danish coast). The results from ROMS on the shelf compare well with the higher-resolution NEMO results. Only a difference of 0.77 cm is found before the Belgian, Dutch and Danish coast. Our results show that with using the relatively low resolution ROM ROMS comparable improvements as with the higher resolution ROM NEMO can be obtained for the GCM sea-level projections in the coastal regions of Belgium, the Netherlands and Denmark. Allowing dynamical downscaled sea-level projections for the coastal area of Belgium, The Netherlands and Denmark with a relatively low resolution ROM reduces computational time.

Contents

List of Abbreviations

AMOC	Atlantic Meridional Overturning Circulation
AO	Arctic Oscillation
AOGCM	Atmosphere-Ocean General Circulation models
CMIP5	Coupled Model Intercomparison Project phase 5
CMIP6	Coupled Model Intercomparison Project phase 6
ENSO	El Niño-Southern Oscillation
GCM	Global Climate Model
GMSL	Global Mean Sea Level
GSL	Geocentric Sea Level
GSLC	Geocentric Sea Level Change
MDT	Mean Dynamic Topography
NAO	North Atlantic Oscillation
NWES	Northwestern European Shelf
ODSLC	Ocean Dynamic Sea-Level Change
ODSLCmIB	Ocean Dynamic Sea-Level Change minus IB-effect
PDO	Pacific Decadal Oscillation
RAM	Regional Atmosphere Model
RCM	Regional Climate Model
RCP	Representative Concentration Pathways
ROM	Regional Ocean Model
ROMS	Regional Ocean Modelling System
SLC	Sea-Level Change
SSH	Sea Surface Height
SROCC	Special Report on the Ocean and Cryosphere in a Changing Climate
SSS	Sea Surface Salinity
SST	Sea Surface Temperature
SSP	Shared Socio-economic Pathway
ToE	Time of Emergence

Chapter 1

Introduction

Since the industrial revolution the emissions of greenhouse gasses have increased, which influences the current climate. The sea level is one of the many climate variables that is influenced by climate change. The the sea level change is of interest for societies living in coastal areas, as an increase in sea level can for example increase the chance of flooding (Oppenheimer et al., 2019). Therefore it is important to observe the sea level and understand what is driving the changes. Already hundreds of years tide gauges measure the sea level along the coast. However not along all coastal areas is the density of data always sufficient. Since 1993 altimetry data is a new source of sea-level information. This highly increases the worldwide data coverage. Beside observing current sea level, projections are made to provide policy makers with information for the future. This information about future sea level is important to have enough adaptation time for possible changes in the protection of communities against the ocean.

For these policy makers it is important they have information about the sea level in their region, because this can deviate from the global mean value. Projections of the relative sea-level change (SLC) (sea level measured above the local solid surface (Gregory et al., 2019)) show deviations up to 30% above or 50% below the global mean (Church et al., 2013) (Figure 1.1). These deviations can be caused by dynamical processes, movements of the sea floor and changes in the gravity due to water redistribution (melt of land ice or changes in the terrestrial water storage) in the climate system (Church et al., 2013). In this study we focus on dynamical downscaling of the sea-level projections made with Global Climate Models (GCMs), included in the Coupled Model Intercomparison Project phase 5 (CMIP5), for the Northwestern European Shelf (NWES) region (Section 1.1). Dynamical downscaling allows to make regional simulations on a higher resolution model compared to the coarse grid size of the GCMs. With GCMs not all contributions as summed up above can be simulated, but only the effects included in the stereodynamic SLC (Gregory et al., 2019). Previous studies have shown the influence of dynamical downscaling (Mathis et al., 2013; Hermans, Tinker, et al., 2020; Liu et al., 2016; Zhang et al., 2017) (Section 1.2).

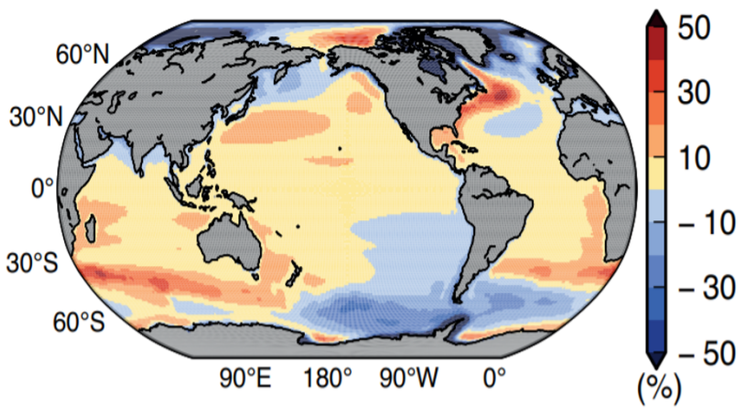

Figure 1.1: The percentage of the deviation of the ensemble mean regional relative sea-level change between 1986–2005 and 2081–2100 compared to the global mean value. This figure shows the results for RCP4.5 (Section 2.5.1), but to first order is representative for all RCPs (Church et al., 2013) This is figure a from Figure 13.21 of (Church et al., 2013).

1.1 The Northwestern European Shelf region

The area of interest for this research is the Northwestern European Shelf (NWES) region. The NWES region is an area with a highly populated coast and is economically dependent on its coastal area.

The solid black line in Figure 1.2 gives the 200 m isobath and indicates the shelf area. It can be seen that the shelf has a steep slope towards the deeper surrounding ocean. The grey arrows indicate the general circulation on the shelf, with water entering the shelf in the south flowing trough The English Channel, The Irish Sea and along the Irish west coast. In the northeast, water enters trough the area around the Orkney Islands, Shetland Islands and through the Norwegian Trench.

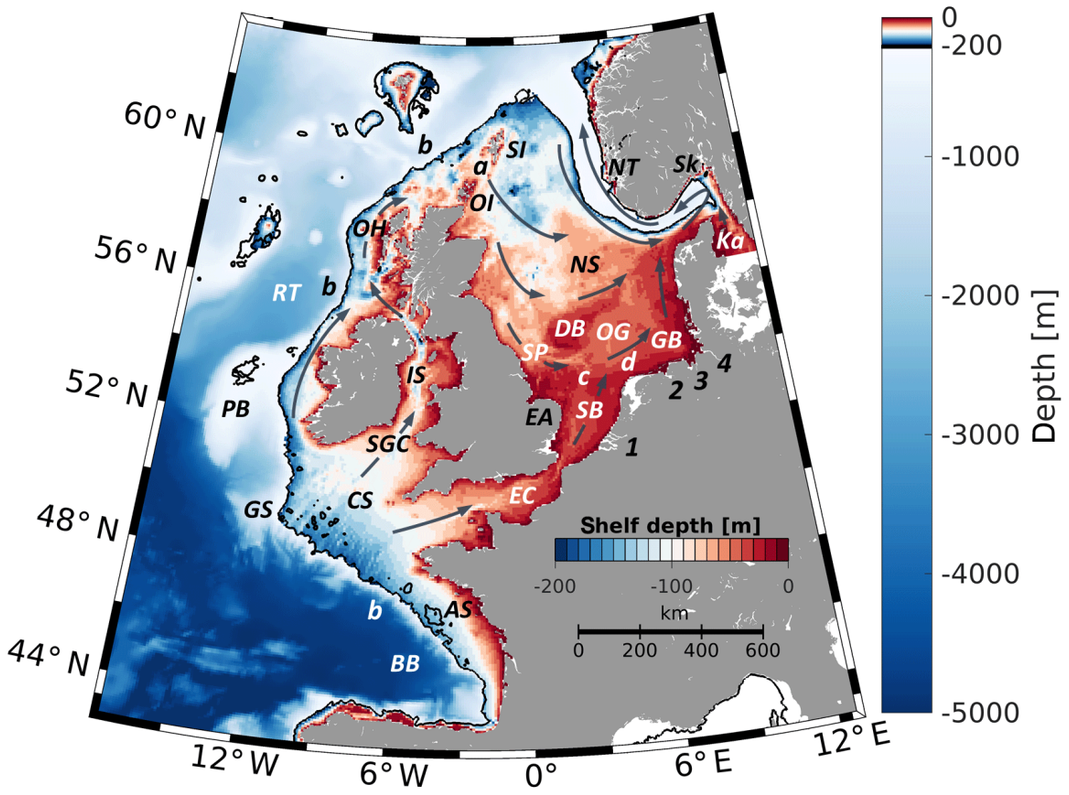

Figure 1.2: The bathymetry of the NWES and the deeper surrounding ocean. The solid black line gives the 200 m isobath delimiting the NWES (colorbar within the map). Grey arrows schematically show the general shelf sea circulation. The abbreviations show the: Armorican Shelf (AS), Bay of Biscay (BB), Celtic Sea (CS), Dogger Bank (DB), East Anglia (EA), English Channel (EC), German Bight (GB), Goban Spur (GS), Irish Sea (IS), Kattegat (Ka), North Sea (NS), Norwegian Trench (NT), Oyster Ground (OG), Outer Hebrides (OH), Orkney Islands (OI), Porcupine Bank (PB), Rockall Trough (RT), Skagerrak (Sk), Southern Bight (SB), St. George's Channel (SGC), Shetland Islands (SI), Silver Pit (SP), Fair Isle Current (a), European Slope Current (b), East Anglia Plume (c), Frisian Front (d), Rhine (1), Ems (2), Weser (3), and Elbe (4) (Ricker & Stanev, 2020).

The main geostrophic current in the area is the Atlantic Current, entering in the southwestern part of the region. The Atlantic Current flows along the shelf and transforms into the Norwegian current leaving the domain in the North east following along the Norwegian coastline northward. The Atlantic Current current enters the shelf on different sides. The largest inflow of the Atlantic current into the North Sea is via the deeper bathymetry of the Norwegian Trench south of Norway (Winther & Johannessen, 2006). Around 50% of the North Atlantic Current that enters the North Sea is mixed with fresher water before it leaves as the Norwegian Coastal Current (Winther & Johannessen, 2006). The Norwegian Coastal current flows from the Skagerrak along the Norwegian coast into the deeper ocean. The mixing of the Atlantic water occurs for a large amount in the inner part of the Skagerrak, but also with river outflow along the coastlines (Winther & Johannessen, 2006). The Skagerrak connects the North Sea via the Kattegat to the fresher water of Baltic Sea. The Baltic Sea freshwater input is considerably large compared to river run-off into the North Sea (Quante et al., 2016).

1.2 Previous studies on dynamical downscaling sea-level projections

For dynmical downscaling a regional ocean model (ROM) is used and forced with GCM data. The CMIP5 GCMs can be forced with different representative concentration pathways (RCPs), furher discussed in Section 2.5.1. The method of dynamcial downscaling has been used already in several studies to make projections of different climate parameters, however for regional sea-level projections the number of studies is limited. Dynamical downscaling to make regional sea-level projections for the NWES region has only been done by (Mathis et al., 2013) and (Hermans, Tinker, et al., 2020). In other geographical regions dynamical downscaled projections have been made by (Liu et al., 2016)

and (Zhang et al., 2017).

Mathis et al. (2013) presents North Sea mean sea-level projections from 1951-2100. Here the HAMSOM ROM is used for dynamical downscaling the CMIP3 generation ECHAM5/MPIOM GCM. The simulations are done on a quasi-orthogonal spherical grid with a horizontal grid size of ~ 3 km. There is a maximum depth of 700 m devided in 30 depth levels. On the lateral boundaries MPIOM GCM data is used and on the atmospheric boundary downscaled ECHAM5 data with the regional atmospheric circulation model REMO is used. They found that the North Sea mean sea-level had a 0.1-0.2 m offset compared to the total global mean sea-level. This shows the importance of making regional sea-level projections for the North Sea.

Hermans, Tinker, et al. (2020) shows the influence of dynamical downscaling for sea-level change projections of the twenty-first century on the NWES. The projected ocean dynamic sea-level change is determined by the difference in the time mean between 1980-2005 and 2074-2099 for a RCP8.5 scenario. For the sea-level projections the regional shelf seas model NEMO AMM7 (1/15° latitude by 1/9° longitude) is used to dynamical downscale the CMIP5 GCMs HadGEM2-ES and MPI-ESM-LR. The atmospheric component of the GCMs is dynamically downscaled with the regional atmospheric model RCA4 and is used on the atmospheric boundary. On the lateral boundaries the ocean component of the GCMs is used. This study has shown that the dynamical downscaled sea-level projections for the twenty-first century differ from a few centimeters (MPI-ESM-LR) up to 15.5 cm (HadGEM2-ES) compared with the GCM projections on the shelf.

In the North Pacific dynamical downscaling using the Regional Ocean Modelling system ROMS (0.25° by 0.25° resolution) has been preformed by (Liu et al., 2016). For the boundary conditions three different CMIP5 GCMs are used: MIROC-ESM, CSIRO-Mk3.6.0 and GFDL-CM3. The dynamical downscaled projections compared to the GCMs all have a difference of less than 10 cm along the Honshu coast for the RPC8.5 scenario. Meaning that the regional sea level along the Honshu coast can be determined with the CMIP5 output considering a 10 cm (extra) uncertainty. However for some islands in the domain larger differences between downscaled output and CMIP5 models are found.

Zhang et al. (2017) uses the near-global ocean model OGCM (1/10°) to dynamical downscale a ensemble of 17 CMIP5 GCMs to make dynamically downscaled sea-level projections for Australia. They define the dynamical sea level as the regional sea-level change deviation from the global mean. The dynamical sea-level signal along the Australian coast is relatively low (within $\pm$ 6 cm). They found for the RCP8.5 scenario that the difference between the GCM and dynamical downscaled results are within $\pm$ 3 cm for the coast. When combining the global mean sea level with different contributions, they find the main source of the regional variations of the total sea level is the dynamical sea level. The regional deviations can be determined to the first order by the dynamical sea level under the RCP8.5 scenario.

The dynamical downscaling set-up of (Mathis et al., 2013), (Hermans, Tinker, et al., 2020) and (Liu et al., 2016) have been validated by comparing historical simulations to observations. For the NWES have the validation results of (Mathis et al., 2013) and (Hermans, Tinker, et al., 2020) shown that dynamical downscaling increases the agreement with observations compared to GCM output. Mathis et al. (2013) has shown this for the sea surface salinity (SSS), sea surface temperature (SST) and the means surface flow. For (Hermans, Tinker, et al., 2020) the increased agreement between the dynamical downscaled simulations and the observations compared to the GCMs is found for the SSS, SST, mean dynamic typography (MDT), annual- and seasonal sea-level variability.

1.3 Research questions

The studies of (Mathis et al., 2013) and (Hermans, Tinker, et al., 2020) discussed in Section 1.2 show the importance of dynamical downscaling the sea-level projections on the NWES region. Compared to the observations have both studies shown an improvement of the simulations when dynamically downscaled. We also have seen in both studies that the dynamical downscaled sea-level projections of the twenty-first century show differences with the the GCM projections. From all four studies discussed in Section 2.5.2, (Liu et al., 2016) uses a relative coarse grid size of the ROM. Focusing on the NWES only higher resolution ROMs have been used. For this research we will use a relatively low resolution grid and simple dynamical downscaling set-up for the ROM ROMS to investigate the influence of this on the sea-level projections. This allows us to investigate the influence of the resolution of the ROM and complexity of the dynamical downscaling set-up. Because the set-up requires less computational power than higher resolution models, the results can be of interest for future dynamical downscaling projects. Especially because projections will in general be made of an ensemble of climate models, meaning that the dynamical downscaling procedure has to be applied to multiple models. So a faster dynamical downscaling set-up can make an important difference in simulation time for dynamical downscaling an ensemble of GCMs. Here we will use one GCM model

to test the influence of dynamical downscaling with the relative low resolution and simple dynamical downscaling set-up for the ROM ROMS.

Our model set-up will be validated by comparing the simulations to observations. Additionally, the influence of dynamical downscaling with the new set-up will be compared to the GCM simulation. Finally, using similar forcing as is done in one of the simulations by (Hermans, Tinker, et al., 2020) allows to compare the results of ROMS and NEMO AMM7 (a higher resolution ROM and a more complex dynamical downscaling set-up). We chose to use the GCM HadGEM2-ES as the forcing for the ROMS model, because the influence of dynamical downscaling of HadGEM2-ES on sea-level projections is large (Hermans, Tinker, et al., 2020).

The research question below captures the goal of our dynamical downscaling set-up. Three sub-questions will be used as a framework to answer the main question:

- What is the influence of dynamical downscaling a GCM (HadGEM2-ES) with the ROM ROMS in the NWES region on the twenty-first century sea-level projections ?
    1. How do the historical dynamical downscaled simulations with ROMS compare with observations?
    2. Which differences and similarities are seen in the dynamical downscaled sea-level simulations compared to the HadGEM2-ES simulations?
    3. Which differences and similarities are seen in the dynamical downscaled sea-level simulations with ROMS compared to previous downscaled simulations using NEMO AMM7?

1.4 Report outline

In the remainder of this report we, will discuss: the theory of the different components that influence the sterodynamic SLC and how the sterodynamic SLC can be determined from (dynamical downscaled) GCM simulations (Chapter 2). Our regional ocean modelling set-up do we introduce in Chapter 3. In Chapter 4 the results of the dynamical downscaled simulation with the ROMS model are shown. A summary of the performance of the ROMS simulations compared to observations, HadGEM2-ES and NEMO, to anwser our research questions, will be given in Chapter 5. Finally, we will conclude if there is a future for dynamical downscaling with ROMS and which improvements or further investigations have to be done for this (Chapter 6).

Chapter 2

Theory of sterodynamic sea-level change

In this chapter we discuss the processes influencing the stereodynamic sea level. The stereodynamic SLC consist of (Gregory et al., 2019):

$$\begin{aligned}\text{stereodynamic SLC} \;=\; &\text{steric SLC (global thermosteric SLC + local steric SLC)} \\ &+ \text{ manometric SLC } + \text{ IB-effect} \end{aligned} \tag{2.1}$$

All the different components will be discussed below: steric SLC (Section 2.1), manometric SLC (Section 2.2) and the IB-effect (Section 2.3). The influence of the spatial and temporal variability on sea-level will be discussed in Section 2.4. Finally, modelling the components of the sterodynamic SLC will be discussed (Section 2.5).

2.1 Steric sea-level change

Steric SLC is caused by changes in the ocean water density. If the water mass is assumed to be constant and the density changes it results in a change in sea level. A higher (lower) density causes contraction (expansion) of the water, so the sea-level falls (rises). These changes in density can be either caused by a change in temperature (thermosteric) or a change in salinity (halosteric) of the ocean water. The ocean temperature and salinity can for example be influenced by: river run-off, precipitation, evaporation or ocean circulation. Sea-level change due to temperature and salinity are respectively known as thermosteric SLC and halosteric SLC. The steric SLC is given by the depth integral of the density change and equals the sum of the thermosteric and halosteric SLC:

$$\Delta R_\rho = \frac{1}{\rho^*} \int_F^\eta \Delta\rho dz = \Delta R_\theta + \Delta R_s \tag{2.2}$$

Here ΔR_ρ is the steric SLC, ρ^* the constant ocean density for the vertical and time mean density, $\Delta\rho$ the change in the ocean density, F the sea floor height, η the mean sea level, ΔR_θ the thermosteric SLC and ΔR_s the halosteric SLC (Gregory et al., 2019).

On shelf regions the steric effects are small compared to the deep ocean (Landerer et al., 2007b). This is explained by the integral in Equation 2.2, as the difference between the mean sea level η and the sea floor height F is relatively small.

2.1.1 Global thermosteric sea-level change

Since the late nineteenth century the global mean temperature has increased (Hartmann et al., 2013). If the emissions of greenhouse gasses are not reduced it is expected that the temperature will keep increasing over the twenty-first century (Collins et al., 2013). In at least the past 1500 years the global mean temperature rise has been the main cause of SLC, which includes ice mass loss and thermal expansion (Oppenheimer et al., 2019).

Temperature having such a large influence on the ocean is explained by the large heat storage in the ocean. Over the past decades more than 90% of the energy increase on Earth has been stored in the ocean (Oppenheimer et al., 2019). Most of the energy has been stored in the upper part of the ocean (0 - 700 m) which accounts for 64% of the heat change between 1971-2010. In comparison, the atmosphere only accounts for 1% of the heat change between 1971-2010 (Rhein et al., 2013).

The deep ocean is a large source of uncertainty. Especially below 2000 m the number of observations is scarce (Rhein et al., 2013). Also in climate models the deep ocean can cause uncertainty as the time to reach a quasi-equilibrium is thousands of years and often longer than the spin-up time of the models (Melet & Meyssignac, 2015). This long time to reach an equilibrium for the deep ocean makes that the adjustment to climate forcing is very slow. Even if the forcing would stay equal, the sea-level rise will still continue for centuries to millennia (Rhein et al., 2013).

The thermal expansion of the ocean is proportional to the heat uptake. However this proportionality is depending on the heat distribution of the ocean, because at higher temperature or under higher pressure the thermal expansion per degree Celsius is larger (Church et al., 2013). Together with local high or low heat uptake compared to the mean this causes regional variation in themosteric SLC (van de Wal et al., 2019).

Thermal expansion together with glacier melt has been the dominant contributors of the global sea-level rise in the twentieth century (Church et al., 2013). Projections shown in Figure 3.2 for RCP2.6 and RCP8.5 forcing show that also in the future thermosteric expansion is expected to be one of the primary drivers of GMSL rise (Abram et al., 2019).

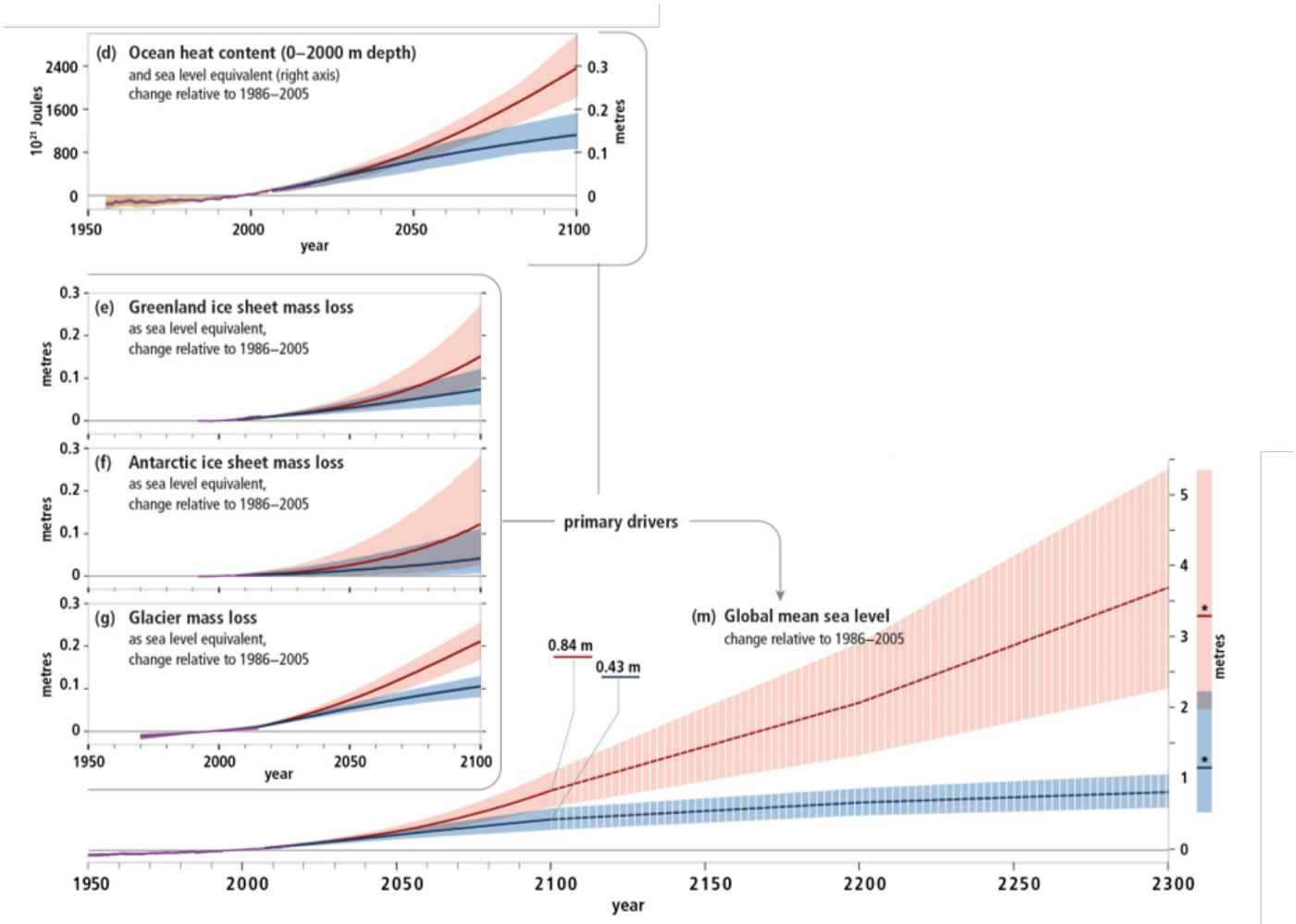

Figure 2.1: The observed and modelled historical changes in the ocean and cryosphere since 1950, and projected future changes under low (RCP2.6) and high (RCP8.5) greenhouse gas emissions scenarios. From the SPM1 figure of (Abram et al., 2019) we show the sea-level changes with likely ranges for: (m) Global mean sea level change. Where the hashed shading reflects low confidence in sea-level projections beyond 2100 and bars at 2300 reflect expert elicitation on the range of possible sea-level change. (d) Global ocean heat content change (0–2000 m depth). An approximate steric sea-level equivalent is shown with the right axis by multiplying the ocean heat content by the global-mean thermal expansion coefficient ($\epsilon \approx 0.125$ m per 10^{24} Joules) for observed warming since 1970. (e,f) Greenland and Antarctic ice sheet mass loss. (g) Glacier mass loss.

2.1.2 Local steric sea-level change

Although the halosteric effect in general is small compared to the thermosteric effect, regionally it can have large influence (Church et al., 2013). As both the temperature and salinity influence the density, the thermosteric effect can be compensated or amplified by the halosteric effect. The Arctic is

one of these areas where thermosteric and halosteric effects compensate each other. Due to increased precipitation, river runoff, melting of sea ice and melt water from the Greenland ice sheet the salinity is lowered and causes halosteric expansion. At the other hand the melt of sea ice lowers the water temperature and causes thermosteric contraction (Yin et al., 2010).

The local steric effect is influenced by ocean circulations which brings water with different temperatures and salinity to new locations. The Atlantic Mederional Overturining Circulation (AMOC) is one of the largest ocean circulations. The AMOC weakens due to the global temperature rise and will affect local steric effects (Li et al., 2016). The wind can influence the ocean circulations and therefore also the local steric sea level. It has been observed that the last half of the twentieth century, the fluctuations of spatial steric patterns in space and time are part of modes of ocean-atmospheric systems, like the El Niño-Southern Oscillation (ENSO), North Atlantic Oscillation (NAO) and Pacific Decadal Oscillation (PDO) (Church et al., 2013).

For the NWES region alongshore winds have influence on the sea level. When the winds are directed northward (going) alongshore winds cause Ekman transport driving surface water towards the coast. The water than subsides at the coast, leading to a deeper thermocline which increases the sea level (Vermeersen et al., 2018). Gerkema & Duran-Matute (2017) has correlated the annual wind energy for eight wind directions (measured at Vlieland) with the annual mean sea level (measured in Den Helder). They found a high positive correlation with the southwesterly and westerly wind directions, while very negative in easterly direction.

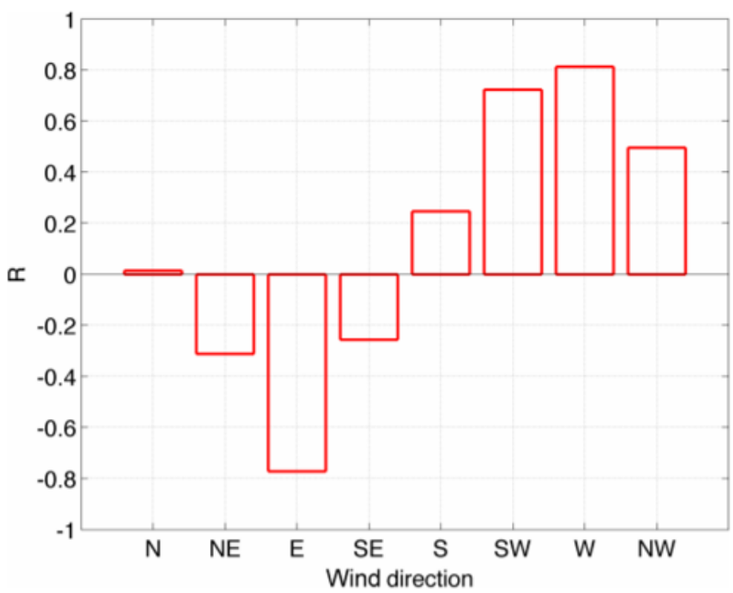

Figure 2.2: The correlation coefficient (R) (based on a 20-year record), giving the correlation between the annual mean sea level (measured in Den Helder) the annual wind energy (measured at Vlieland) for eighth different directions: northerly (N), northeasterly (NE), easterly (E), southeasterly (SE), southerly (S), southwesterly (SW), westerly (W), and northwesterly (NW). This is the direction from which the wind blows. (Gerkema & Duran-Matute, 2017)

A source of freshwater into the oceans are rivers. Besides a lower salinity the river inflow will in general also have a different temperature compared to the ocean. This makes that river inflow can both affect the thermosteric and the halosteric effect. One of the largest rivers in Europe, the Rhine, enters the North Sea at Rotterdam. It has its headwaters in the European Alps, so changes in the European Alps will also influence the runoff into the North Sea (Stahl et al., 2016). In (Hock et al., 2019) findings of studies researching the river runoff (of the European Alps) of past decades and projected changes are discussed: Over the past decades the winter runoff of the European Alps has increased due to increased precipitation falling as rain because of increased warming. The summer runoff has decreased for the European Alps. These trends are region dependent and also for future projections the changes depend on the regional circumstances. For most snow/glacier-fed regions, including the European Alps, it is projected that the winter run off will increase. On the other hand the projections for the summer runoff show a decline. For the annual mean run off of the European Alps it is projected that the peak water (the turning point from the increased runoff to the decline in runoff due to shrinking glaciers) is before or around halfway the twenty-first century. For regions with larger ice cover and larger glaciers the peak water will in general be reached later. These changes in the runoff can influence the local steric sea level, however it needs to be taken into account that the river run-off in the North Sea is considerably small compared to the Baltic Sea inflow Quante et al. (2016).

Sterlini et al. (2017) has used a reanalysis data set, based on the Forecasting Ocean Assimilation Model 7 km Atlantic Margin Model, to calculate the thermosteric and halosteric effect in the North Sea. The local steric sea-level trend anomalies in Figure 2.3 show that the thermosteric and halosteric anomaly sometimes have opposite signs, for example in the southeastern part of the North Sea. This will cause the local thermosteric and halosteric effect to partly cancel each other out. On the other hand along the Norwegian coast both the local themosteric and halosteric linear trend is positive. So along the Norwegian coast the thermosteric and halosteric effect do amplify each other.

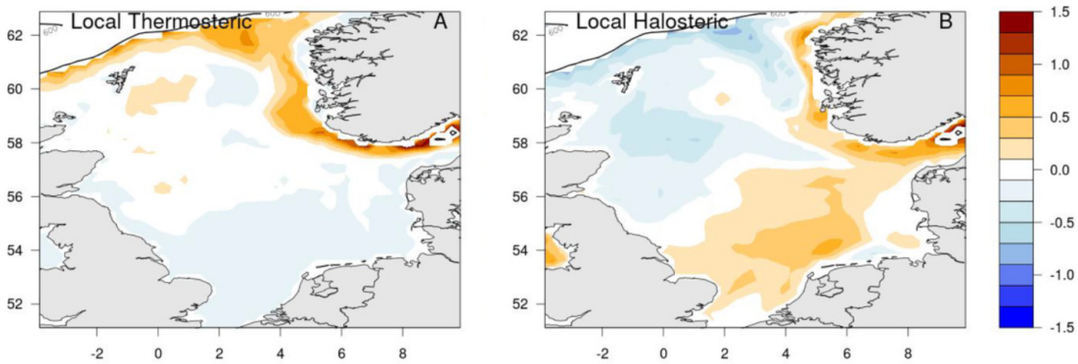

Figure 2.3: Local (left) thermosteric and (right) halosteric regional linear sea-level trend anomalies, 1993–2013 (mm/yr). Data beyond the 600 m depth contour are not plotted (Sterlini et al., 2017).

2.2 Manometric SLC

The manometric SLC is the change of mass per unit area with a zero global mean (Gregory et al., 2019). The change in manometric SLC is influenced by the local steric SLC. As discussed in Section 2.1 is the steric effect on the shelf small compared to the deeper oceans. If this cannot be compensated by for example geostrophic flow it will cause mass from the deeper ocean to flow onto the shelf area (Landerer et al., 2007b; Yin et al., 2010).

2.3 Inverse barometric effect

Atmospheric pressure can influence the height of the sea surface. For the GMSL change the influence of the atmospheric pressure can be neglected as the ocean is nearly incompressible. A uniform change of 1 hPa in the atmosphere will cause the GMSL to rise with 0.16 mm (Gregory et al., 2019). However due to regional deviations from the global mean sea level pressure water is moved around. If we look at timescales of a few days or longer, hydrostatic pressure can be assumed. Further is the spatial and temporal variation of of the gravitational acceleration and surface sea-water density about 1%, therefore (for most peruses of sea-level studies) these can be replaced by constants (Gregory et al., 2019). The time-dependent hydrostatic depression of the sea surface height (SSH) by atmospheric pressure variations is defined as the inverted barometer (IB) by (Gregory et al., 2019), often also referred to as the inverse barometer effect (IB-effect). The depression of the SSH by IB is given by (Equation 2.3):

$$\tilde{B} = \frac{\tilde{p_a}'}{g\rho_*} \tag{2.3}$$

Here $\tilde{B}$ is the depression of the SSH by the IB-effect, $\tilde{p_a}'$ is the deviation of the sea-level pressure for the global mean, g the gravitational acceleration and ρ_* a constant surface sea-water density (Gregory et al., 2019).

By a regional increase (decreas) in the sea-level pressure of 1 hPa the regional SSH will go down (up) with 10 mm (Equation 2.3) (Stammer & Hüttemann, 2008). Church et al. (2013) shows that the IB-effect over the twenty-first century is small for low- and mid latitudes (Figure 2.4. For the NWES in Figure 2.4 a sea-level fall of 50 mm is projected.

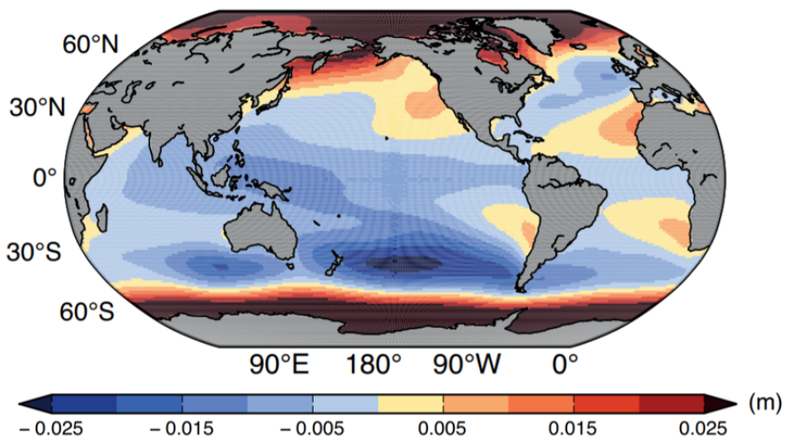

Figure 2.4: From Figure 13.17 (Church et al., 2013) we show panel b: Projected ensemble mean sea level change due to changes in atmospheric pressure loading over the period from 1986–2005 to 2081–2100 for RCP8.5.

2.4 Variability in sea level in space and time

The climate is a very variable system on all different lengths of timescale. There are changes on a small time scale, the weather tomorrow will be different than today, and on really large time scales as also glacial periods cause variability. Besides variability over time, climate variability can also cause large spatial differences. Over decadal periods, the rates of regional SLC due to climate variability and the global average rate of SLC can differ more than 100% (Church et al., 2013). Variability can be caused by either internal or external sources. Internal variability is induced by the system itself. Examples of internal variability are ENSO or changes in circulation systems (Church et al., 2013). External variability can be caused for example by changes in radiative forcing, volcanic eruptions or human activity. The largest differences in sea level are between glacial and interglacial periods. During the last glacial maximum the sea level has been around 120 meter below present day (Fairbanks, 1989). The current moment of iteration between glacial and interglacial periods is called Quanternary and started 2 to 3 Ma ago (Berger & Yin, 2012). The main forcing behind the variation between glacial and interglacial is astronomical (Berger & Yin, 2012). Since the last 1 Ma the glacial cycle has a period of 100 ky (Muller & MacDonald, 1997). The time frame for climate projections is centuries, which means that the variability with the timescale of glacial periods can be neglected. However, past records can give information about sea level in comparable climate circumstances that might be faced in the future. In the warm intervals of the middle Pliocene, Marine Isotope Stage 11 and The Last Interglacial Period the temperature was a few degrees higher than pre-industrial and the GMSL was up to multiple meters above present day (Church et al., 2013). On the other hand, sea-level projections in general use mean values over a time period which at least cancels out weather fluctuations (Gregory et al., 2019). For sea-level projections, variability of seasonal, interannual, decadal and multi-decadal timescale are of most interest.

In climate models external forcing of volcanic eruptions, changes in solar irradiance and anthropogenic increases in greenhouse gasses and aerosols are taken into account. Besides external variability also internal variability is simulated in the models, by climate modes such as ENSO, PDO and NAO that are into account (Section 2.4.1). For sea-level projections made with climate models the natural variability can be determined from simulations. Which only includes the variability of the sea-level components included in the GCMs. In the study of (Lyu et al., 2014) they used a 200 year time series, of a linearly de-trended pre-industrial control run, as reference period to determine the noise from. It needs to be taken into account that internal variability in climate models can be statistically the same as observations, but does not occur at the same time (Goosse, 2015).

2.4.1 Sea-level variability on the NWES

Variability is an important concept for sea-level projections. It can complicate the determination of possible trends in projections (Gerkema & Duran-Matute, 2017; Frederikse & Gerkema, 2018). In Section 2.4.1 the sea-level variability taking place on the NWES is discussed. Time of emergence (ToE) of sea level gives a measure when a trend can be distinguished from variability in sea-level data and is discussed in Section 2.4.2.

The sea level on the NWES is strongly affected by atmospheric changes, as the water depth is shallow

and the atmospheric variability is large (Dangendorf, Rybski, et al., 2014). The NAO is major source of interannual variability in the atmospheric circulation and associated with surface westerlies over the North Atlantic onto Europe (Hurrell, 1995). In winter the NAO is the strongest and the interannual variability the greatest (Wakelin et al., 2003). The strength of the NAO is given by the NAO index which is traditionally defined by the mean sea level pressure difference between Iceland and the Azores (Rogers, 1984). Wakelin et al. (2003) and Tsimplis et al. (2005) use the date set of (Jones et al., 1997) where the NAO index is defined by the difference between the normalized sea level pressure over Gibraltar and southwest Iceland to be able to extend the data in time. The correlation between the mean-winter NWES tide+surge model elevation and the NAO index has a clear spatial pattern: in the northeast it is larger than 0.8 (Figure 2.5), while the correlation in the south east is smaller than -0.7. This corresponds with the fact that a positive NAO index induces low (high) atmospheric pressure in the north (south) which leads to increase (decrease) of sea level due to the hydrostatic changes (Wakelin et al., 2003).

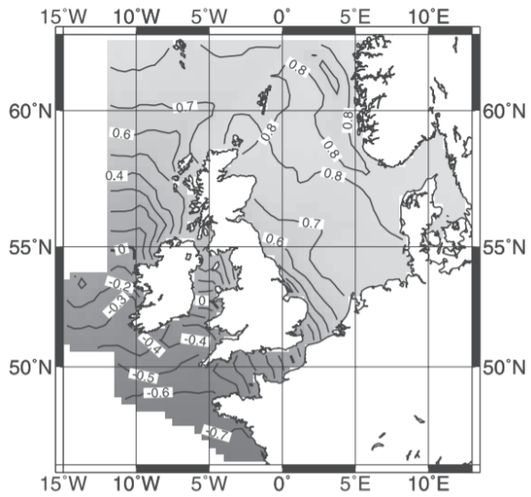

Figure 2.5: Correlation coefficient between the winter-mean NAO index and the winter-mean tide + surge model elevation (Wakelin et al., 2003).

Figure 2.6 shows the correlation between the NAO index and the simulated winter-mean sea level for when (a) wind and atmospheric pressure variations are included as forcing and (b) only wind is included as forcing. It can be seen that sensitivity of the North Sea is wind dominated. The southeast and north of the NWES are pressure dominated (Tsimplis et al., 2005). Further, the NAO index is also positively correlated with air temperature, wind speed, relative humidity and precipitation for the north side of the NWES (Mathis et al., 2013).

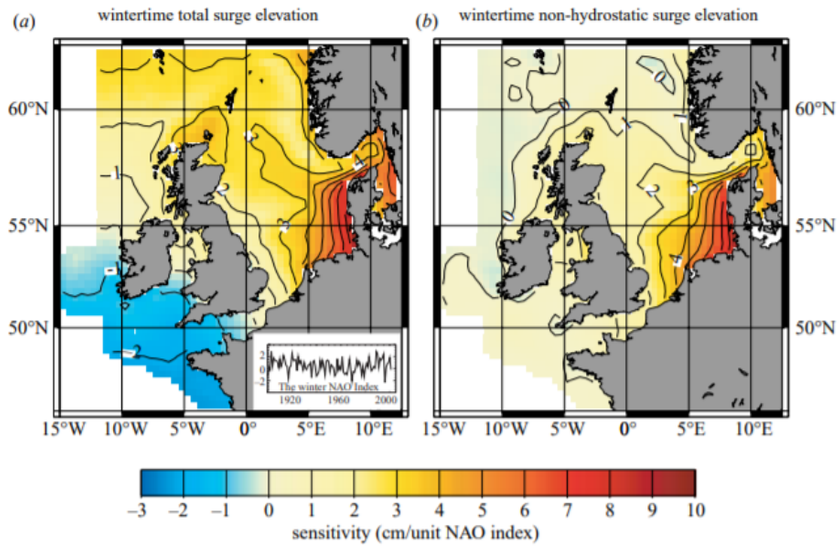

Figure 2.6: Sensitivity of the sea-level elevation to the winter-mean NAO index in mm/(unit NAO index). (a) The winter-mean tide+surge model elevations and (b) the winter-mean tide+surge model elevations corrected for hydrostatic pressure (IB-effect correction) (Tsimplis et al., 2005).

It is of interest if the relation between the NAO and the sea level of the NWES will change under changing climate conditions. Wakelin et al. (2003) found that the correlation between the mean-winter

tide+surge model elevation and the NAO index increased for 1980-2000 compared to 1959-1979. Simulations with 7 GCMs under enhanced carbon dioxide by (Tsimplis et al., 2005) have shown that there is no consistent change in the relation between the NAO index and sea level between the different models. Atmospheric pressure patterns of other circulations will interfere with each other and the NAO causing a non-stationary relation between sea level and the NAO (Vermeersen et al., 2018). Jevrejeva et al. (2005) and Papadopoulos & Tsimplis (2006) show that also the Arctic Oscillation (AO) winter-mean index has a large influence on the sea level of the NWES. The AO index itself is also highly correlated with the NAO index (Jevrejeva et al., 2005).

There is also variability on longer timescales, which influences the sea level on the NWES. Frederikse & Gerkema (2018) show that the NAO, East Atlantic Pattern and Scandinavia Pattern all cause multi-decadal variability. Also for this low-frequency variability the winter- and autumn-mean variability is larger than the summer- and spring-mean variability (Frederikse & Gerkema, 2018).

The timescales of variability caused by different sources differs. Dangendorf, Calafat, et al. (2014) shows that the sea-level variability as response to local sea-level pressure and wind acts on a intra- and interannual time scale. For the region from the Belgium coast up to the Danish coastline the variability is mainly dominated by wind. This is in agreement with (Tsimplis et al., 2005) (Figure 2.6b). Spatially is the interannual variability in the North Sea well correlated. Especially from the Belgium, Dutch, Danish and Norwegian coast and slightly weaker with the eastern English coast. However the correlation of most places in the North Sea with the English Channel is weak (Wahl et al., 2013). On decadal scale the variability is more similar for different stations around the North Sea. The variability due to the sea-level pressure and wind becomes negligible on decadal time scale. The main source therefore are probably longshore winds causing a displacement of the thermocline leading to coastally trapped waves (Dangendorf, Calafat, et al., 2014).

2.4.2 Time of emergence

The ToE is a measure to indicate a trend in observations or simulations. The definition of the ToE given in the Special Report on the Ocean and Cryosphere in a Changing Climate (SROCC) glossary is: 'Time when a specific anthropogenic signal related to climate change is statistically detected to emerge from the background noise of natural climate variability in a reference period, for a specific region' (Hawkins & Sutton, 2012) (Figure 2.7). The exact definition of the ToE and how the variability of the reference period is determined differs for different studies. Lyu et al. (2014) investigated the ToE for sea level and for example defined the ToE as the time when the ratio of the climate signal and natural variability exceeds a specific threshold and never falls below that threshold. With extra criterion: the ToE has to last for a minimum of two decades. They found that the moment when the ToE is reached is depends on which sea-level change contributions are taken into account. When only dynamical sea-level contributions are considered only a small fraction of the ocean will emerge above the natural variability in 2080 under a high emission scenario. While taking all the sea-level contributions into account nearly all of the ocean will reach the ToE before 2080 (Lyu et al., 2014).

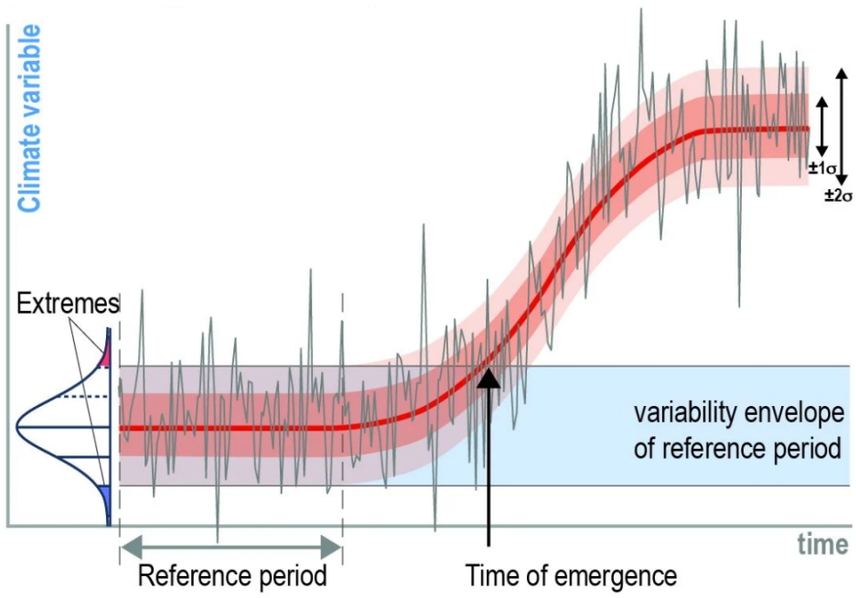

Figure 2.7: Figure (b) Variability, Time of Emergence and Extremes of Figure 1.1 from Abram et al. (2019). It shows the evolution of a dynamical system in time, revealing both natural (unforced) variability and a response to a new (e.g., anthropogenic) forcing. Further extremes near or beyond the range of variability are indicated. (Abram et al., 2019).

It is important for the ToE that the reference period is long enough to make sure that low frequency

variability is not considered as a trend. This could happen if only variability on a short time scale (e.g. interannual and shorter) is subtracted from a signal. Variability on the longer time scale (e.g. decadal time scale) can be mistakenly considered as a trend. The importance to take the right length scale of data to determine the ToE is indicated by (Frederikse & Gerkema, 2018) where they found that multi-decadal seasonal sea-level variability is of the same order of magnitude as the long term trend in mean sea level.

Hermans, Tinker, et al. (2020) showed how dynamical downscaling can be used to determine the ToE on the NWES for the sterodynamic SLC. They found that dynamical downscaling can cause a delay in the ToE of the sterodynamic SLC of up to 12 years. This occurred for simulations where the difference between the dynamical downscaled simulations and the GCM for the ODSLC over the twenty-first century was less than 2.5 cm. So although the difference at the end of the century is small the effect on dynamical downscaling can be large due to the difference in sea-level variability and timing of the SLC for the ROM and the GCM. Further they found that the ToE of the German Bright was late compared to the rest of the North Sea due to high local internal variability.

2.5 Modelling sterodynamic SLC

The sterodynamic SLC can be determined from simulations with the GCMs. We discuss the GCMs included in CMIP5 and the simulations that can be used to determine the different components included in the sterodyanmic SLC (Section 2.5.1). In Section 2.5.2 we explain how the GCM simulations can be dynamically downscaled.

2.5.1 CMIP5 global climate models

There are a lot of different GCMs we will focus on the GCMs included in the Coupled Model Intercomparison Project phase 5 (CMIP5). The GCMs used in CMIP5 are nearly all Earth System Models, which expand the Atmosphere-Ocean General Circulation models (AOGCMs) by including a representation of the biochemical cycles. The AOGCMs describe the dynamics of the physics in the climate system (atmosphere, ocean, land and sea ice) (Flato et al., 2013). The GCMs are used to simulate climate parameters and make projections of these parameters based on increasing greenhouse gas. There are a lot of different GCMs which are designed and run by different institutions. These models are constantly under development and for each new CMIP phase improved versions are used. At the moment of writing all output of CMIP5 (Taylor et al., 2012) and part of the output of the new phase, CMIP phase 6 (CMIP6) (Eyring et al., 2016) is available.

Climate models need a set of input values consisting of forcing data and initial data. To make sure the output of the different models is comparable the same forcing needs to be used. There are multiple sets of forcing input which are linked to scenarios that can describe what might happen in the future. For CMIP5 Representative Concentration Pathways (RCPs) are used to force the simulations. The RCPs are based on land use and emissions of greenhouse gasses and air pollution's (O'Neill et al., 2016). The four different RCPs, cover 1850 until 2100 resulting in a radiative forcing of 2.6, 4.5, 6.0 and 8.5 W/m^2 in 2100 with extensions until 2300 (van Vuuren et al., 2011). From 1850 until 2005 historical forcing is used for all four scenarios, meaning that from 2005 onward the forcing will deviate depending on the scenario used (Figure 2.8).

There can be multiple realisations for different ensembles with the same scenario. Before the models are able to generate data about the future, there is a spin-up time, a control run and a historical run. For the spin-up and control run pre-industrial forcing is used. The spin-up data will not be saved, the control run is used to provide initial states for the runs (Figure 2.8) (ENES PORTAL, 2019). Besides forcing data the models also need initial conditions to make the simulation. The model branches of the pre-industrial control run at different points (Figure 2.8) (called realization). The realization (the initial state), initialisation and physics are grouped in ensembles. These ensembles are indicated with rip-nomenclature r#i#p#, where the '#' numbers behind the r, i and p indicate respectively the realization, initialisation and physics.

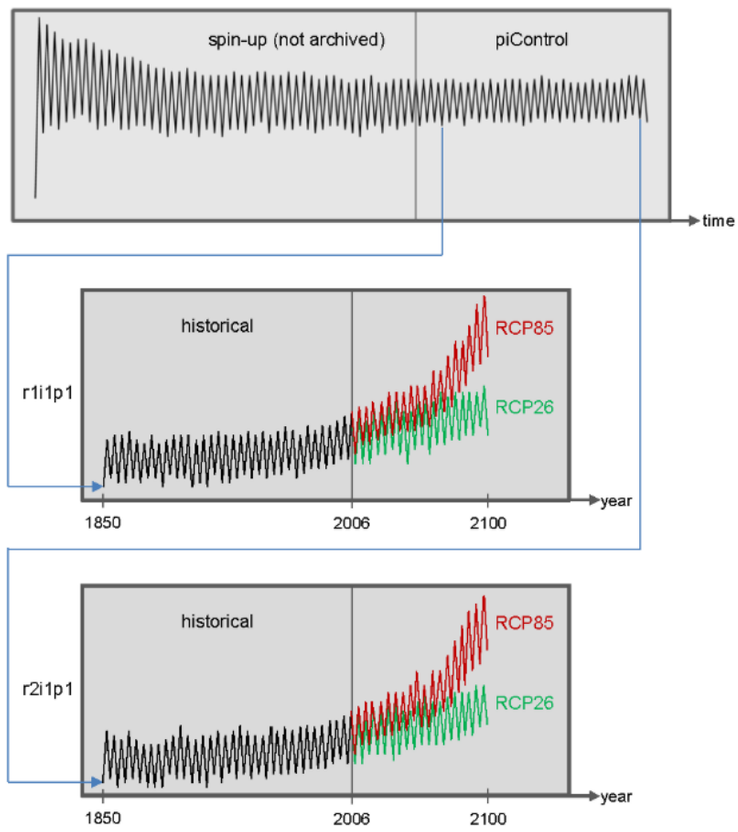

Figure 2.8: Schematic overview of the different type of GCM runs. On top the spin-up and the control run, which provides different realizations, used as initial state for the other simulations. In the middle and bottom the runs for two different realizations, showing the historical run and the results for RCP2.6 and RCP8.5. (ENES PORTAL, 2019).

Simulations with a GCM for an ensemble of different initial conditions gives an indication of the uncertainty due to the internal variability of the model. Where the physics ensemble is used to systematically estimate the uncertainty in the simulation. Both these ensemble runs give information about an individual GCM. Multi-model ensemble runs, where all models from the different institutions included in the CMIP are run, indicates the uncertainty of the simulation. Selection criteria can be used to weight some models more than others. The weights will be based on the expected ability of the model to perform better compared to other models (Knutti et al., 2010). In general an multi-model ensemble run is preferred for presenting projections on which decisions are based, because the simulations are not dependent on the performance of a single model.

As said before not all contribution to SLC are included in the GCMs. The contributions to the sterodynamic SLC (Chapter 2) can be determined from the output of the GCMs, however it has to be calculated from multiple variables (Gregory et al., 2019). The first GCM variable is the sea level measured above the geoid saved as 'zos'. This is equal to the sum of the local steric sea level and the manometric sea level. The second variable is the global thermometric SLC saved as 'zostoga'. The global thermometric SLC is determined separately, because the GCMs conserve, due to the Boussinesq approximation, volume rather than mass. Zostoga is determined from the change in the spatial mean density. Finally, the atmospheric pressure variable can be used to calculate the IB-effect. So the sterodynamic SLC determined form the GCM is (Equation 2.4):

$$\begin{aligned}\text{stereodynamic SLC} \;=\; &\text{zos (local steric SLC + manometric SLC)} \\ &+ \text{ zostoga (global thermosteric SLC)} \;+\; \text{IB-effect} \end{aligned} \tag{2.4}$$

If only the variable 'zos', the local steric SLC + manometric SLC, is considered including the IB-effect this is defined as the ocean dynamic sea-level (ODSL) (Gregory et al., 2019) change (Equation 2.5):

$$\text{ocean dynamic SLC (ODSLC)} \;=\; \text{zos (local steric SLC + manometric SLC)} \;+\; \text{IB-effect} \tag{2.5}$$

As the information of the various variables is calculated over the entire globe the resolution is relatively coarse, due to computational restrictions. The coarse resolution makes GCMs less well suited for (sea-level) projections of certain (coastal) regions, because processes at a scale smaller than the resolution cannot be captured.

2.5.2 Dynamical downscaling

To obtain information on a higher resolution regional climate models (RCMs) can be used. Compared to GCMs, RCMs typically operate on a finer horizontal grid size with more depth levels, so they have a higher resolution. The RCMs only cover a limited region, which requires less computational power compared to the GCMs. The RCMs can be used to dynamically downscale the GCM results to obtain higher resolution results. There are separate RCMs for the ocean (ROM) and the atmosphere (RAM). For dynamical downscaling sea-level projections a ROM is used. The ROM has open boundaries and needs boundary conditions on the lateral boundaries and the surface boundary. Figure 2.9 shows the set-up of dynamical downscaling a GCM with a ROM. As shown in the figure, on the lateral boundary ocean variables are needed and on the surface boundary atmosphere information is required. On the surface boundary it is possible to use atmospheric data that is previously dynamically downscaled with a RAM. For the different ocean and atmosphere variables it is important to use the same ensemble (rip-nomenclature). When the output of the GCM is used only on the boundaries of the RCM it is called "one-way nesting". It is also possible to use "two-way nesting" where the RCM provides feedback to the GCM.

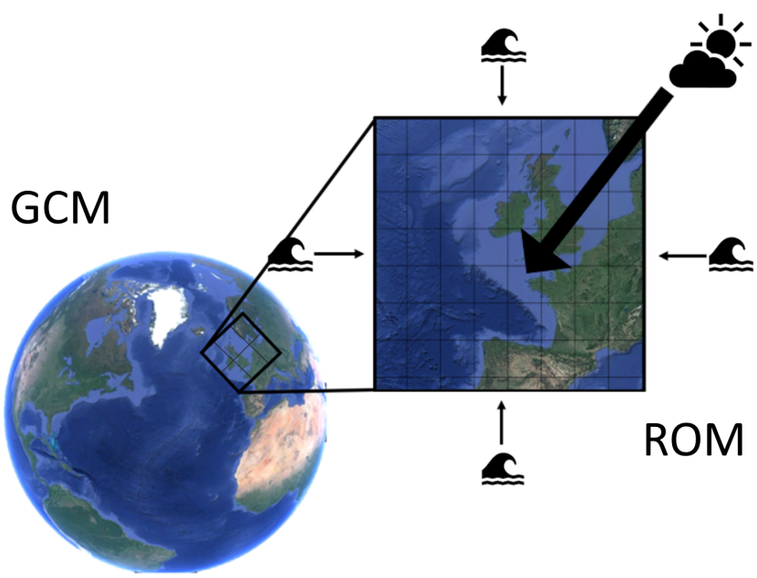

Figure 2.9: Dynamical downscaling ("one-way nesting" approach) GCM output with a ROM. GCM output is prescribed on the lateral and surface boundaries. (Images of Google Earth Pro are used to make this figure.)

For making sea-level projections with a 3D ROM, in general the variables SSH, temperature, salinity, u- and v-velocity components of the GCM ocean component need to be prescribed. For the SSH the variable 'zos' of the GCM can be used. This gives the dynamical downscaled projections of the local steric SLC + manometric SLC, which we will refer to as the ocean dyanmic sea-level change minus IB-effect (ODSLCmIB). Offline the global thermometric SLC (zostaga) and the IB-effect can be added. The effect of prescribing the sum of 'zos' and 'zostoga', as SSH boundary conditions to a ROM, on the dynamical downscaling results has not yet been studied. In this study we will focus at the ODSLCmIB.

Chapter 3

Regional ocean modeling

We dynamical downscale a single CMIP5 GCM HadGEM2-ES with the ROM ROMS. We introduce these models in Section 3.1, followed by the boundary conditions of the dynamical downscaling set-up where the forcing of the ROMS model is described in more detail (Section 3.2). Further we discuss the mass conservation correction (Section 3.3) and the data dynamically downscaled with the ROM NEMO from the previous study (Hermans, Tinker, et al., 2020) (Section 3.4).

3.1 Downscaling HadGEM2-ES with ROMS

HadGEM2-ES is one of the CMIP5 GCMs. The model uses a 360 day calendar (12 months consisting of 30 days) and has a regular horizontal grid. The resolution of the ocean component is 1°by 1°($\sim$ 100 km) for the NWES region (Met Office, 2020). Due to the coarse horizontal resolution the land mask as seen in (Figure 3.1b) misses some of the characteristics of the NWES land mask: The channel between England and French does not exist, Ireland and England are presented as one piece of land and there is no connection between the North Sea and the Baltic Sea as the area between Norway and Denmark is filled with land. Further shows Figure 3.1b also that the bathymetry is influenced by the low horizontal resolution, specifically around the shelf area. Here steep changes in the bathymetry can not be resolved. So is the Norwegian Trench not represented in the HadGEM2-ES bathymetry. The HadGEM2-ES ocean component has 40 vertical depth levels. On the shelf the maximum depth is approximately 200 meter. There are only 17 levels are above 200 meter depth. The HadGEM2-ES simulation data used in this research are forced with the RCP8.5 and from the ensemble r1i1p1.

The ROMS model is used to dynamical downscale the simulations of the HadGEM2-ES model. For this study a ROMS set-up available at the NIOZ has been used and adapted to perform dynamical downscaling. ROMS is based on the equations described in Appendix A. ROMS is a complex model and has many options. For this research the settings of the model are used as tested for previous simulations in the NWES region (Hermans, Le Bars, et al., 2020), but with a 1/4° by 1/4° horizontal resolution and adjusted where needed. The main adjustments are: the domain of the simulation (Section 3.2.1) and the type of calendar, which is set to a 360 day calendar (the same calendar type as the HadGEM2-ES forcing). In the settings used tides are not considered. The domain of the simulation is 39.8° N by 62° N and 20° E by 10° W which allows to solve the exchange between the deeper ocean and the shelf internally in the ROMS model, but excludes the the Skagerrak and Kattegat from the domain. The ROMS model has a curvlinear grid of 1/4° by 1/4° ($\sim$ 20 km). There are 30 terrain-following s-levels in depth. Unlike the HadGEM2-ES model, where a maximum of 17 of the 40 depth levels cover the shelf, the shelf of the ROMS model will be covered by 30 depth levels. This allows the ROMS model to solve processes on the shelf such as vertical mixing processes and the bottom boundary layer better compared to HadGEM2-ES. Further does the higher resolution of ROMS capture the topography better, as can be seen in Figure 3.1a. For example is the Norwegian Trench present in the ROMS bathymetry. The bathymetry data in the ROMS model is derived form ETOPO1 (Amante & Eakins, 2009). The bathymetry is smoothed to reduce the slope steepness between the shelf and the deep ocean to reduce possible numerical errors, causing the shelf to become slightly smaller than originally. The model is run in parallel on the NIOZ Laplace High Performance Cluster for the period 1972-2098. From what the first 8 years are used as spin-up and not used in the results. We chose this period to be able to compare the ROMS sea-level projections with the sea-level projections of NEMO for the twenty-first century. The run ends 2098 instead of 2099, because the forcing used ends in 2099 which does not allow the ROMS model to run until 2099.

The data of both models will be presented on their native grids, to maintain the characteristics of the models. Differences are calculated and presented on the ROMS grid. For regridding the HadGEM2-ES data bilinear interpolation is used. The data cells that were originally land are filled with nearest neighbor interpolation.

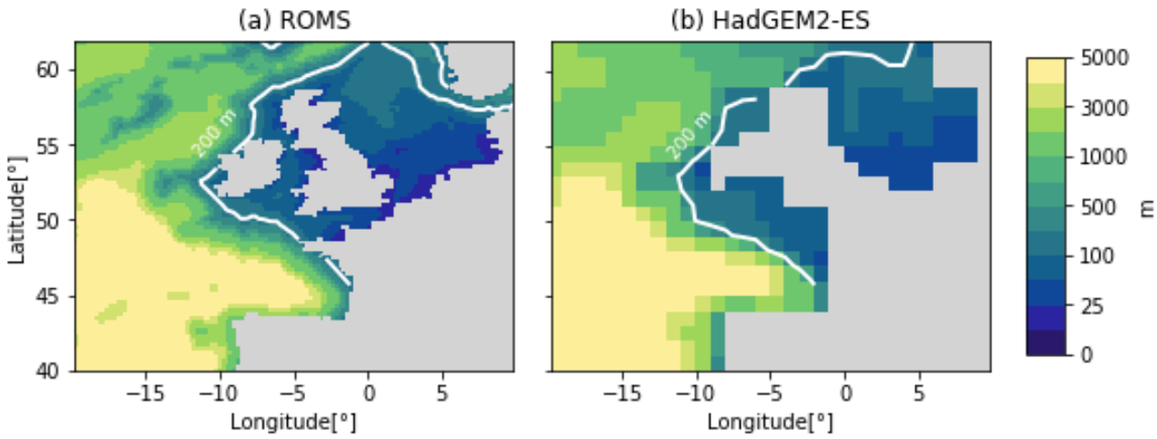

Figure 3.1: The land mask (in grey) and bathymetry (with the 200 m isobath in white) of (a) the ROMS model and (b) the HadGEM2-ES model.

3.2 Boundary conditions of the dynamical downscaling set-up

In the ROMS model different types of boundary conditions can be selected for the different ocean variables. For the free surface we impose the Champman implicit (Chapman, 1985), for the 2D momentum components the Flather (Flather, 1976) and for the 3D momentum components, temperature and salinity the mixed-radiation nudging (Orlanski, 1976) (Marchesiello et al., 2001) boundary conditions. Nudging causes the variables to slowly run to the forcing data, to make sure the values in the ROMS model will not go to far of the GCM data. By (Marchesiello et al., 2001) it is advised to use a weak outgoing nudging, to prevent for substantial drifts while avoiding problems due to over-specification, and a stronger in going nudging, while making sure it does not cause a data shock. We use a 1 year timescale for the outgoing nudging and a 1 day timescale for the in going nudging. For the temperature and salinity a 10 point relaxation-zone is used. The 3D momentum components are only nudged at the boundaries. To dampen potential instabilities in the model a 10 point sponge is used where the viscosity and diffusivity linearly increase towards the boundary. This linearly increasing viscosity lets possible flow decay close to the boundaries, while the high diffusivity close to the boundary decreases differences in temperature and salinity between grid cells. To apply the atmosphere forcing bulk fluxes are used based on (Fairall et al., 1996).

To dynamical downscale the HadGEM2-ES data the HadGEM2-ES ocean component is prescribed on the lateral boundaries of the ROMS model. On the ROMS surface boundary, dynamical downscaled HadGEM2-ES atmosphere data is prescribed. The forcing data for the surface- and lateral boundaries are prescribed in a "one-way nesting" approach and respectively introduced in Section 3.2.1 and 3.2.2. In the dynamical downscaling set-up a climatological river inflow is prescribed (Section 3.2.3). Here we will also discuss the Baltic Sea inflow in the ROMS model in more depth.

3.2.1 Atmospheric forcing

On the surface boundary of the ROMS model the atmosphere HadGEM2-ES data dynamical downscaled with the RAM Rossby Centre regional atmospheric model (RCA4) (Rossby Centre, 2020) from the Coordinated Downscaling Experiment - European Domain (EURO-CORDEX) simulations is used (EURO-CORDEX, 2020). Besides an increased spatial resolution, the frequency of the available Eurocordex data is also higher compared to the frequency of the available HadGEM2-ES atmosphere component. The higher resolution and frequency of the forcing data is expected to benefit the simulations. We want to prescribe the atmospheric forcing on a 6 hour frequency, because we assume it captures the influence of the daily cycle on the variables sufficiently. A lower frequency causes a less realistic simulation by possible not resolving a day and night cycle in the atmospheric data, which may influence the results. On the other hand a higher frequency will take more computational time. For the the annual results we will be looking at, it is not expected using a higher frequency makes a significant difference.

The downscaled atmosphere data are on an irregular 0.11° by 0.11° grid with rotated poles. Since ROMS is not able to regrid the complex gird of the Eurocordex data, we directly regrid the atmosphere data onto the ROMS grid using bilinear interpolation and rotate the wind to the North and East directions of the curvilinear ROMS grid. The domain that the Eurocordex data does not cover the entire domain as used in the set-up of (Hermans, Le Bars, et al., 2020), therefore the southern boundary is shifted slightly northward from 36°N to 39.8°N.

The variables prescribed on the surface boundary of ROMS are listed in Table 3.1, with the HadGEM2-ES variables that are used. Some of the variables needed unit conversion and the net solar shortwave radiation is calculated form the surface downwelling and upwelling shortwave radiation. The Eurocordex wind data is downloaded on a 6 hour frequency, the other variables are downloaded on a 3 hour

frequency (6 hour frequency was not available). All variables except the radiation has been prescribed every 6 hour. As can be seen in Table 3.2 the moment of prescribing the data is not the same for all variables as the moment of prescribing was inherited from the Eurocordex data. For solar radiation a daily average was derived. The radiation is prescribed to ROMS on a daily frequency, because an idealized daily radiation cycle is used. The longwave radiation is internally calculated as a function of air temperature, sea surface temperature, relative humidity and cloud fraction (Wiki ROMS, 2020).

HadGEM2-ES variable	**HadGEM2-ES unit**	**ROMS unit**	**ROMS variable**
Eastward Near Surface Wind (uas)	m/s	m/s	surface u-wind component (at 10 m)
Northward Near Surface Wind (vas)	m/s	m/s	surface v-wind component (at 10 m)
Total Cloud Fraction (clt)	%	0 - 1	cloud fraction
Sea Level Pressure (psl)	Pa	mbar	surface air pressure
Near-Surface Air Temperature (tas)	K	C	surface air temperature (at 2 m)
Near-Surface Relative Humidity (hurs)	%	%	surface air relative humidity (at 2 m)
Surface Downwelling Shortwave Radiation (rsds) Surface Upwelling Shortwave Radiation (rsus)	W m-2 W m-2	W m-2	solar shortwave radiation flux
Precipitation (pr)	kg m-2 s-1	kg m-2 s-1	rain fall rate

Table 3.1: Atmospheric variables HadGEM2-ES with the units used to provide the ROMS forcing variables needed in the correct units. The abbreviations of the HadGEM2-ES variables, as they can be found in the data bases, are given inside the parenthesis. For the surface wind components, surface air temperature and surface air relative humidity the height at which they are prescribed are given in parenthesis.

ROMS atmosphere frocing variable	**Moment of prescribing forcing variable on a day**
surface u-wind component	00:00, 06:00, 12:00, 18:00
surface v-wind component	00:00, 06:00, 12:00, 18:00
cloud fraction	01:30, 07:30, 13:30, 19:30
surface air pressure	00:00, 06:00, 12:00, 18:00
surface air temperature	00:00, 06:00, 12:00, 18:00
surface air relative humidity	00:00, 06:00, 12:00, 18:00
solar shortwave radiation flux	12:00
rain fall rate	01:30, 07:30, 13:30, 19:30

Table 3.2: Atmospheric forcing variables ROMS with the time the the forcing is prescribed.

3.2.2 Ocean forcing

For the lateral boundaries the monthly HadGEM2-ES ocean component is used. The ocean data is used to generate initial conditions, boundary conditions and climatology data sets. The intital conditions are needed to start the simulation, the boundary conditions are given in files with the variables for the northern, southern, western and eastern boundary and the climatology files are used for nudging. These three data sets are generated with the python toolbox model2roms (Kristiansen, 2020) available on GitHub, which also regrids the data on to the ROMS grid.

Table 3.3 shows the forcing variables with the units needed for the ROMS model and the corresponding HadGEM2-ES variables that are used. Only for the potential temperature a unit conversion is needed. The vertically integrated momentum components are calculated in the model2roms toolbox using the 3D momentum components. All variables are prescribed at 00:00 on the 16th of the month.

HadGEM2-ES variable	**HadGEM2-ES unit**	**ROMS unit**	**ROMS variable**
sea-surface height above geoid (zos)	m	m	free-surface
sea water x velocity (uo)	m s-1	m s-1	3D u-momentum component
sea water y velocity (vo)	m s-1	m s-1	3D v-momentum component
		m s-1	vertically integrated u-momentum component
		m s-1	vertically integrated v-momentum component
sea water potential temperature (thetao)	K	C	3D potential temperature
sea water salinity (so)	PSU	PSU	3D salinity

Table 3.3: Ocean variables HadGEM2-ES with the units used to provide the ROMS forcing variables needed in the correct units. The abbreviations of the HadGEM2-ES variables, as they can be found in the data bases, are given inside the parenthesis.

The zos value from HadGEM2-ES is corrected for the global area-weighted mean zos of HadGEM2-ES. The gobal mean zos field should be zero by definition, however due to model drift it can occur that the global mean zos field is non-zero.

3.2.3 River- and Baltic Sea inflow

For the river run-off we use a climatology based on the river discharge data set from (Dai, 2017). The climatology data varies during the year, but is the same for every year. So there will be no interannual variability due to freshwater inflow from rivers. The water inflow is assumed to be purely freshwater. The Baltic Sea is closed off in the HadGEM2-ES model while open in the ROMS model. Due to the closure of the Baltic Sea in the HadGEM2-ES model is the interchange between the water off the Baltic Sea and the North Sea not taken into account. In this simulation we choose to use the regridded data from HadGEM2-ES and not prescribe any in-/outflow at boundary. This means that also in the downscaled simulations the in-/outflow with the Baltic Sea is not considered, even though the ROMS land mask suggests that they are connected. Although a prescribed in-/outflow of the Baltic Sea would make the simulation more realistic, it would also make the dynamical downscaling set-up more complex.

3.3 Mass conservation correction

Both the ROMS and HadGEM2-ES model use the Boussinesq approximation, which implies that volume is conserved. This causes that if the spatial mean density changes the mass in the system changes as well, which causes a physical spurious change. As this can cause a change in mass while there is a zero mass flux on the lateral boundaries. This will not occur in the real ocean (Griffies & Greatbatch, 2012). The GCMs have closed boundaries and therefore a spatial uniform time dependent correction for the global mean ocean expansion or extraction can be used (Greatbatch, 1994). For the CMIP5 GCMs 'zostoga', the global mean thermosteric SLC, can be used as the correction for the spurious bottom pressure change. Therefore we will present the manometric SLC simulations including 'zostoga'.

ROMS only simulates a limited region (the NWES region) of the total region HadGEM2-ES simulates. Because we use the "one-way nesting" approach, an spurious change in mass in the ROMS model will not cause an decrease in mass in the HadGEM2-ES model. Meaning the total mass of the ocean will increase, which is physically impossible. Further differences in the mass in ROMS model and the mass of the NWES region in HadGEM2-ES can come from boundary conditions of the dynamical downscaling set-up. Discrepancies in the in- and outflow of on the lateral boundaries, due to regridding of the HadGEM2-ES data on the ROMS grid and different atmospheric, river inflow and bathematry representations can also add to discrepancies in the mass flow across the lateral boundaries.

To compare the ODSLCmIB results of HadGEM2-ES and ROMS a correction for the differences in regional mean ODSLCmIB due to the Boussinesq approximation and the dynamical downscaling set-up has to be made. The correction as represented in (Hermans, Tinker, et al., 2020) is used. Here the spatial mean manometric SLC of the RCM is replaced by the regional mean manometric SLC of the GCM:

$$\Delta\eta^{*}_{ROMS}(x,y,t) = \Delta\eta_{ROMS}(x,y,t) - \Delta\overline{\eta}^{P_b}_{ROMS} + \Delta\overline{\eta}^{P_b}_{HadGEM2-ES}(t) \tag{3.1}$$

Where $\Delta\eta^{*}_{ROMS}$ and $\Delta\eta_{ROMS}$, are respectively the corrected and uncorrected ODSCmIB of the ROMS model depending on time and space. $\Delta\overline{\eta}^{P_b}_{ROMS}$ and $\Delta\overline{\eta}^{P_b}_{HadGEM2-ES}$ are the area-weighted mean ODSLCmIB due to bottom pressure changes in the NWES region for ROMS and HadGEM2-ES, respectively.

3.4 Dynmical downscaling set-up with NEMO from (Hermans, Tinker, et al., 2020)

The simulations with ROMS will be compared with dynamical downscaled simulation results from a previous study (Hermans, Tinker, et al., 2020). Here the ROM AMM7 (Coastal ocean version 6) configuration of the primitive-equation modelling framework Nucleus for European Modelling of the Ocean (NEMO) V3.6 (Madec & the NEMO team, 2016) is used from now on referred to as NEMO. The NEMO set-up uses the same forcing data for the lateral- and surface boundaries as the ROMS set-up: the HadGEM2-ES ocean component for the lateral boundaries and for the surface boundary the HadGEM2-ES atmosphere component dynamically downscaled with RCA4. However the forcing data is not in the exact same way prescribed. The atmosphere data is prescribed at a different frequency and direct fluxes are used instead of a bulk formula. Also for the lateral boundaries there is a difference in how the ocean data is prescribed. Other differences are there in the river and Baltic Sea forcing used. The river inflow is prescribed with the Total Runoff Integration Pathways (TRIP) river routing model. Unlike the ROMS model, for NEMO a Baltic Sea in-/outflow is prescribed using a climatology for the temperature, salinity and barotropic currents. The resolution of the NEMO simulation is higher than the ROMS simulation, with a horizontal resolution of 1/15° latitude and 1/9° longitude ($\sim 7\ km$). Also the vertical resolution of NEMO is higher with 50 depth levels compared to the 30 depth levels in ROMS. The domain of the NEMO simulation is 40 ° N by 65 ° N and 20 °

W by 13 ° E, because it reaches further east it allows to capture the Skagerrak and Kattegat. Further does the NEMO model take tides into account while these are not considered in the ROMS model.

Like the HadGEM2-ES and ROMS data will the NEMO data be presented on the native grid, to maintain the characteristics of the model. Also here differences are calculated and presented on the ROMS grid, for regridding bilinear interpolation is used and near neighbor interpolation is used to fill cells that were originally land.

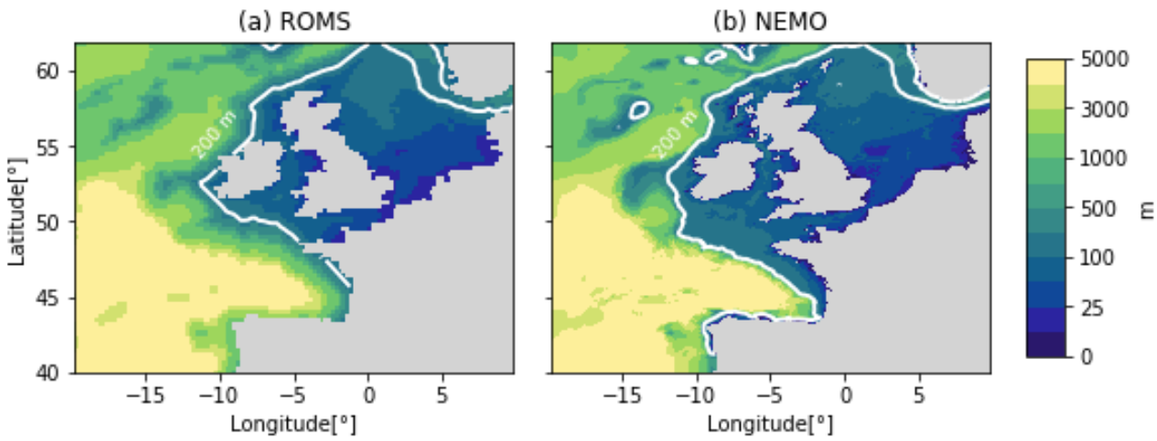

Figure 3.2: The land mask (in grey) and bathymetry (with the 200 m isobath in white) of (a) the ROMS model and (b) the NEMO model.

The NEMO simulations run from 1972 (with first 8 years of spin-up) until 2099 therefore is the time-mean SLC computed as the difference between 1980-2005 and 2074-2099. It is assumed that a one year difference in the period at the end of the century will not have significant influence on the results. (Hermans, Tinker, et al., 2020) presents the ODSLC, so they have added the IB-effect to the simulations. The influence of the IB-effect on the centennial scale is small (Section 2.3). In the study of (Hermans, Tinker, et al., 2020) they found that the difference due to the IB-effect for different models was less than 0.5 cm. So we do expect that the the comparison of the ODSLC of the NEMO model (IB-effect included) and the ODSLCmIB of ROMS (IB effect not included), will be valid. The MDT, local steric SLC and manometric SLC results of NEMO are not correct for the IB-effect. Further is the mass conservation correction applied to the ROMS data the same as is used for the NEMO data.

Chapter 4

Dynamical downscaled simulations with the ROMS model

In this chapter we first compare the historical part of the ROMS simulation with observations to verify the model (Section 4.1), which allows us to answer our first research question. In Section 4.2 we compare the twenty-first century projections of ROMS with HadGEM2-ES and NEMO, allowing us to respond to our second and third research question.

4.1 Model verification

To verify the ROMS set-up we compare the simulations to observations (presented on their native grid). We also compare the HadGEM2-ES data to the observations to show the influence of dynamical downscaling the HadGEM2-ES data with ROMS. For the MDT (Section 4.1.1) also the NEMO simulations are included for the comparison to the observations. In Section 4.1.2 we will look into the interannual variability simulated by the HadGEM2-ES and ROMS model and compare the simulations to the AVISO satellite observations. Finally, the depth averaged temperature and salinity of HadGEM2-ES and ROMS will be compared to reanalysis data (Section 4.1.3). For all simulations we calculate (on the ROMS grid) the spatial correlation (r) and root mean square error (RMSE) compared to the observations to determine how well the simulations perform.

4.1.1 Mean dynamic topography in observations versus model

The mean dynamic topography (MDT) (a measure for mean surface circulations) of the simulations is computed by taking the time mean of the annual mean sea level for the period 1993-2012. We compare our simulations to the MDT CNES CLS18 (Rio et al., 2014) data set, which covers the period 1993-2012. The data set has a global coverage of 1/8° by 1/8° of the mean sea surface above the latest GOCO05S geoid model. The MDT CNES CLS18 data is based on the complete GOCE mission, 10.5 years of GRACE data and 25 years of altimetry and in-situ data (AVIOS+, 2018).

The HadGEM2-ES, NEMO and ROMS MDT anomaly (w.r.t the regional mean) (Figure 4.1a,b,c) all reproduce the negative anomaly in the north-east and positive anomaly in the south-west as in the MDT CNES CLS18 data (Figure 4.1d). This MDT anomaly gradient is perpendicular to the North Atlantic current. The North Atlantic current flows along the shelf break and is a slope current, driven by the horizontal density gradient and the topography (Huthnance, 1984). The spatial correlation of the models versus the observations show an increase of 0.1 between HadGEM2-ES and ROMS. NEMO has a slightly higher spatial correlation compared to ROMS, meaning the MDT anomaly of NEMO correlates the best with the observations. However, the difference between the spatial correlation for ROMS and NEMO is relatively small (0.02) compared to the increase in spatial correlation for ROMS compared to HadGEM2-ES (0.1). Besides the larger spatial correlation, NEMO also has a smaller RMSE, although also this difference is small (1 cm).

The NEMO model captures the MDT anomaly gradient perpendicular to the Norwegian Coastal Current and the inflow of the North Atlantic Current through the Norwegian Trench (Figure 4.1b). In the satellite data (Figure 4.1d) this high anomaly by the Norwegian coast is not as clear as it is in NEMO, this can be because of land contamination which makes the accuracy of the satellite data lower near the coast. The ROMS simulations (Figure 4.1c) show the MDT gradient perpendicular to the North Atlantic Current through the Norwegian Trench. However the positive MDT anomaly along the Norwegian coast is barely visible. This means that the Norwegian Coastal Current is not sufficiently captured in ROMS. This may be caused by the in- and outflow of the Baltic Sea not being sufficiently included in the simulation. This can be due to the not prescribed Baltic Sea inflow, but also the domain not capturing the Skaggerrak and Kattegat and the lower resolution of the ROMS model compared to NEMO may have influenced this. In the ROMS grid the Norwegian Trench is only covered by $\sim$ 4 grid cells, while in NEMO this is $\sim$ 10 grid cells. In the HadGEM2-ES model (Figure 4.1a) the horizontal grid size is too coarse to capture the bathymetry of the Norwegian Trench sufficiently to simulate the anomaly gradient. For the HadGEM2-ES simulation in the North Sea, a

checkerboard like pattern is shown, possibly due to the low resolution causing numerical instabilities in the horizontal diffusivity (Hermans, Tinker, et al., 2020).

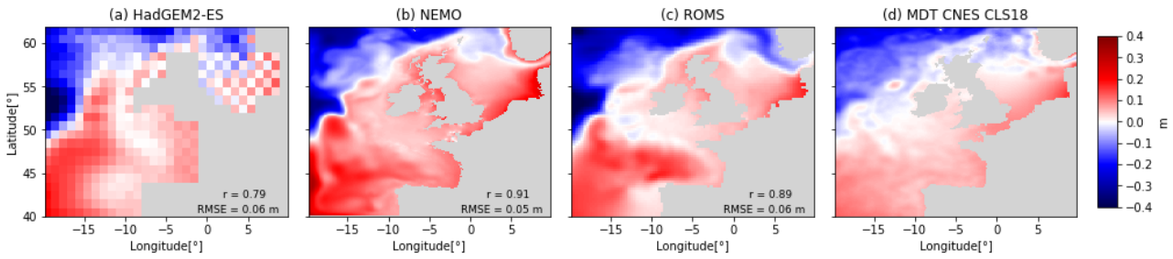

Figure 4.1: The MDT anomaly (w.r.t the regional mean) for the period 1993-2012 of (a) HadGEM2-ES, (b) NEMO, (c) ROMS with in the bottom right the spatial correlation (r) and the root-mean square error (RMSE) of the simulations compared with the (d) MDT CNES CLS18.

4.1.2 Interannual variability in observations versus model

To investigate the performance of the interannual variability of the ROMS and HadGEM2-ES models, a level-4 gridded Ssalto/Duacs satellite product is used (AVISO+, 2018) containing the monthly sea-level anomaly for the period of 1993-2019. The sea-level anomalies are the SSH measured by satellites from which the MDT is subtracted. Furthermore, the data set has been corrected for tides and the IB-effect. In the satellite data, SSH fluctuations due to changes in water storage for example on land or in the atmosphere is included (barystatic sea-level change) (Gregory et al., 2019). We assume that the barystatic sea-level variability on the annual time scale is small (Frederikse et al., 2016).

We compare the standard deviation of the detrended annual mean ODSLmIB for the period 1993-2019 of HadGEM2-ES and ROMS simulations (Figure 4.2a,b) with the Ssalto/Duacs observational satellite product from AVISO (Figure 4.2c) to investigate the interannual variability in the simulations. Compared to the observations the variability of both simulations is relatively high over the entire domain, but especially in the deeper ocean. Where the spatial average over the entire domain for AVISO is 2 cm, for the simulations the spatial average is 3.7 and 3.3 cm for respectively HadGEM2-ES and ROMS. The relative high variability of the simulations is also seen in Figure 4.3, where the standard deviations of HadGEM2-ES (Figure 4.3a) and ROMS (Figure 4.3b) are compared to the standard deviations of the AVISO satellite observations. Here we see that especially the higher simulation values compare poorly with the AVISO data. Mainly these higher standard deviation values for HadGEM2-ES are slightly decreased in ROMS, which are found in the deep ocean. The RMSE of HadGEM2-ES (1.6 cm) decreases slightly after dynamical downscaling with ROMS (1.4 cm). In the study of (Hermans, Tinker, et al., 2020) they also found that dynamical downscaling with the model NEMO cannot completely compensate for the to high variability in the HadGEM2-ES model. Despite the relative high variability in the simulations, we can still see some of the characteristics in the observations back in the simulations. Some of these characteristics that are seen in the observations (Figure 4.2c) are the high variability along the Danish and Dutch coast and the low variability in the Norwegian Trench area. Both the high variability along the Danish and Dutch coast and the lower variability in the Norwegian Trench are also seen in Figure 4.2b for the ROMS simulations. Despite the coarse grid size, the higher variability along the Dutch and Danish coast is also seen in the HadGEM2-ES simulations. Further do we see a relative high variability around the ROMS shelf compared to HadGEM2-ES and the AVISO data, this can be caused by the smaller ROMS shelf due to smoothing (Section 3.1). Over the full domain, the spatial correlation with the observations is 0.1 higher for the HadGEM2-ES model compared to ROMS.

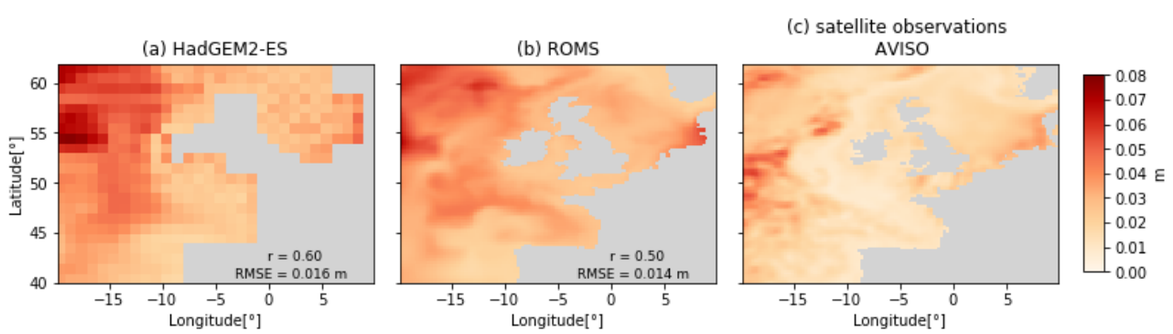

Figure 4.2: The standard deviation for the period 1993-2019 of the detrended annual mean ODSLmIB for (a) HadGEM2-ES and (b) ROMS with in the right bottom the spatial correlation (r) and RMSE of the simulations compared with the (c) AVISO satellite observations.

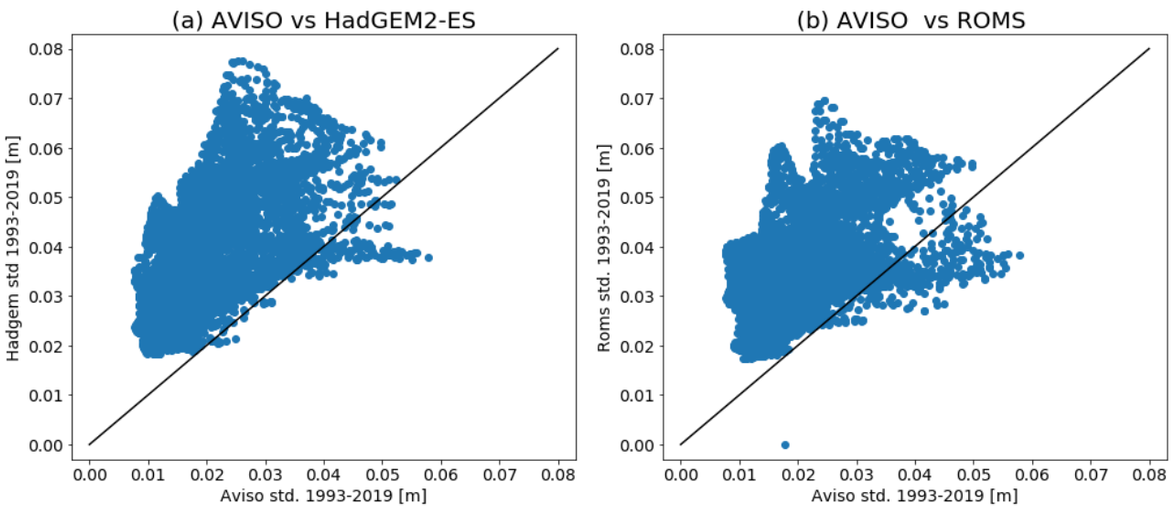

Figure 4.3: (a) the standard deviation (std) of HadGEM2-ES for 1993-2019 versus the std of Aviso data and (b) the standard deviation (std) of ROMS for 1993-2019 versus the std of AVISO data

Richter et al. (2017) has shown that due to the difference in timing of internal variability in the climate models and the observations, the best correlation of the simulations with the observations can differ from the observational period. To investigate if there is another time window for which the interannual variability matches better with the observations we use a sliding time window of 27 years (starting in 1980-2006 and adding a year to the start and end date each time) of the HadGEM2-ES and ROMS simulations to calculate the spatial correlation (Figure 4.4a) and RMSE (Figure 4.4b) of the simulations versus the observations. The differences in the RMSE over time do not show a clear peak (Figure 4.4b). For the spatial correlation (Figure 4.4a) we see some more clear peaks, however there is not a clear time window where both HadGEM2-ES and ROMS perform significantly better. The RMSE of ROMS is always lower compared to HadGEM2-ES. However the spatial correlation of ROMS is initially lower than HadGEM2-ES, but becomes higher than HadGEM2-ES after the time window 2005-2031. In the period 2014-2040, when ROMS has the largest spatial correlation value (0.65), we find that the characteristics of the high variability along the Dutch and Danish coast are present for both HadGEM2-ES and ROMS. There is also still a low variability along the Norwegian coast in the ROMS simulations of 2014-2040. For ROMS the variability around the shelf has become lower, however for both ROMS and HadGEM2-ES also the variability in the deep ocean has changed. The differences in Figure 4.4a are possibly mainly caused by differences in the deeper ocean, because on the shelf of the simulations for the periods 1993-2019 and 2014-2040, where the spatial correlations are respectively 0.50 and 0.65 for ROMS, show the same characteristics and no clear differences.

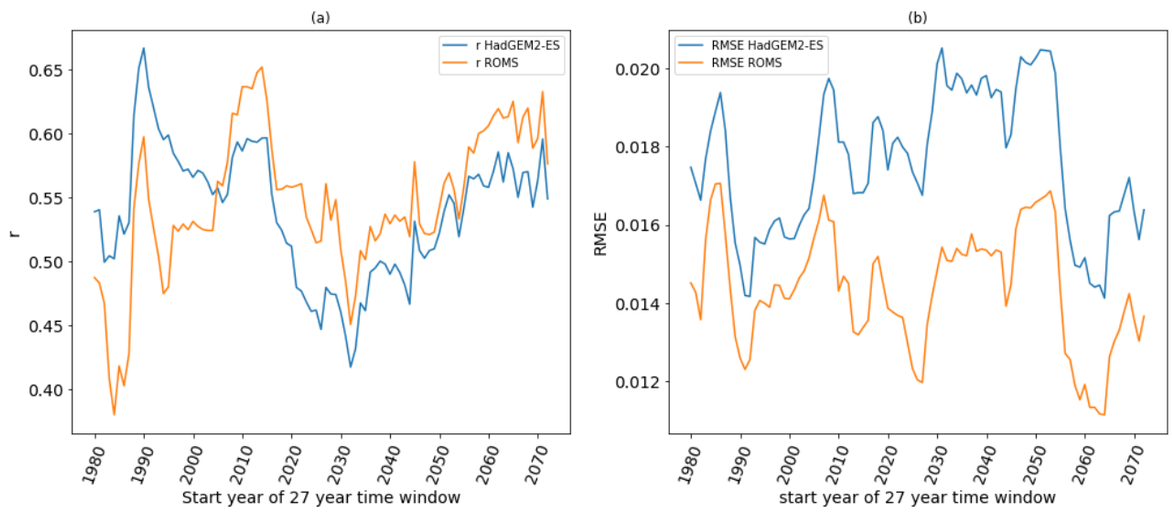

Figure 4.4: For a 27 year sliding time window of HadGEM2-ES and ROMS the (a) spatial correlation (r) and (b) RMSE compared to the AVISO satellite observations.

To determine how the ROMS and HadGEM2-ES simulations compare to AVISO on the continental shelf (the area below the 200 m isobath connected from French to Denmark in Figure 3.1a) we calculate only for this area the spatial correlation and RMSE. This increases the spatial correlation for the period 1993-2019 from 0.50 and 0.60 to 0.65 and 0.68 for respectively ROMS and HadGEM2-ES (Figure 4.5a). The RMSE decreases respectively from 1.4 cm and 1.6 cm to 0.51 cm and 0.46 cm for ROMS and HadGEM2-ES. A clear peak in the spatial correlation is seen for 1990-2016 for both HadGEM2-ES and ROMS (Figure 4.5a). The RMSE is very variable (Figure 4.5b) and therefore we

will use the spatial correlation to determine the best period simulating the interannual variability of the AVISO data. For the period of 1990-2016 HadGEM2-ES had the largest spatial correlation (0.79), ROMS has only a slightly smaller spatial correlation of 0.75, with a respective RMSE of 0.51 cm and 0.50 cm for HadGEM2-ES and ROMS. The results on the shelf for the years 1990-2016 are very similar to the other periods. Therefore it is not clear which characteristic on the shelf increases the spatial correlation off the simulations with the observations. However the analysis for the shelf area has shown that large variability in the deep ocean indeed has a major influence on spatial correlation of the entire domain.

We would have expected the spatial correlation to increase after dynamical downscaling, because we expect the processes in the domain, especially the shelf, to be better captured in ROMS compared to HadGEM2-ES. Further did (Hermans, Tinker, et al., 2020) find an increase in spatial correlation and decrease in RMSE for the interannual variability after dynamical downscaling HadGEM2-ES with NEMO. This could mean that ROMS possibly has a too low resolution, however also the observational data used to compare differs. Hermans, Tinker, et al. (2020) used tide gauge data, meaning they only considered data points of the simulations close to the coast to compare to the tide gauge observations. In the satellite data we used land contamination can have influenced the data points close to the coast, this is the area where we specifically expect ROMS to perform better and therefore can have influenced our results.

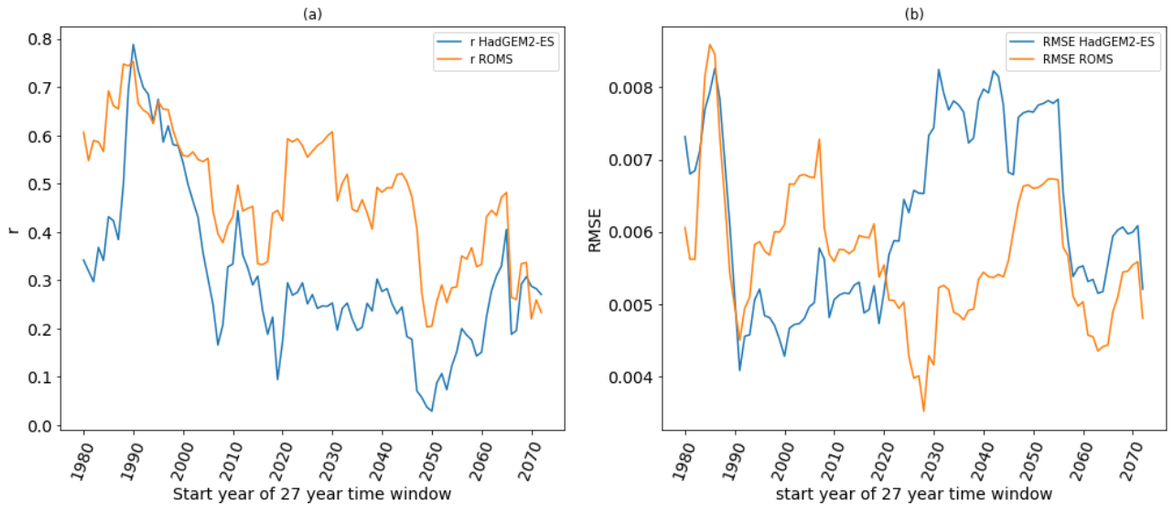

Figure 4.5: For a 27 year sliding time window of region below the 200 m isobath for HadGEM2-ES and ROMS the (a) spatial correlation r and (b) RMSE compared to the AVISO satellite observations.

4.1.3 Temperature and salinity in observations versus model

The temperature and salinity are directly related to the sea level as a result of their effect on the density of the ocean water, causing local steric SLC. The temperature and salinity simulations are compared to the reanalysis data set NORTHWESTSHELF REANALYSIS PHY 004 009 (E.U. Copernicus Marine Service Information, 2020). For this reanalysis data set, the model NEMO, with a 7 km horizontal resolution and including tides, and the 3DVar NEMOVAR system for data assimulation are used. The forcing on the lateral boundary is given by GloSea5 and on the atmospheric boundary by the ERA-Interim atmospheric reanalysis (E.U. Copernicus Marine Service Information, 2020). Temperature and salinity are 3D variables, we consider the depth (weighted) averaged values for the time-mean over 1993-2012. We only consider the ROMS and HadGEM2-ES model here, because in the study of (Hermans, Tinker, et al., 2020) there is no similar analysis done for NEMO.

Figure 4.6 shows that the simulations of the temperature anomaly (w.r.t. the regional mean) in the models and the reanalysis data compare relatively well, with spatial correlation values of 0.85 (HadGEM2-ES) and 0.83 (ROMS). The slightly lower spatial correlation value for ROMS is probably caused by the reduced performance of ROMS in the Norwegian Trench. In the Norwegian Trench the spatial mean positive anomaly of ROMS is 1.74 °C (with the highest anomaly between Norway and Denmark) compared to 0.33 °C in HadGEM2-ES, while the reanalysis data shows a negative anomaly (spatial mean -0.21 °C). Also the difference in the RMSE is small (0.05), showing that the temperature simulations of HadGEM2-ES and ROMS perform relatively similar in comparison to the reanalysis data. Further we find that the spatial correlation on the shelf does not change too much from the full domain with respectively 0.83 and 0.82 for ROMS and HadGEM2-ES. Also the RMSE decreases for both models to 0.32 °C. So also when we focus on the shelf area with in the domain, dynamical downscaling only improves the spatial correlation of the simulations with 0.01.

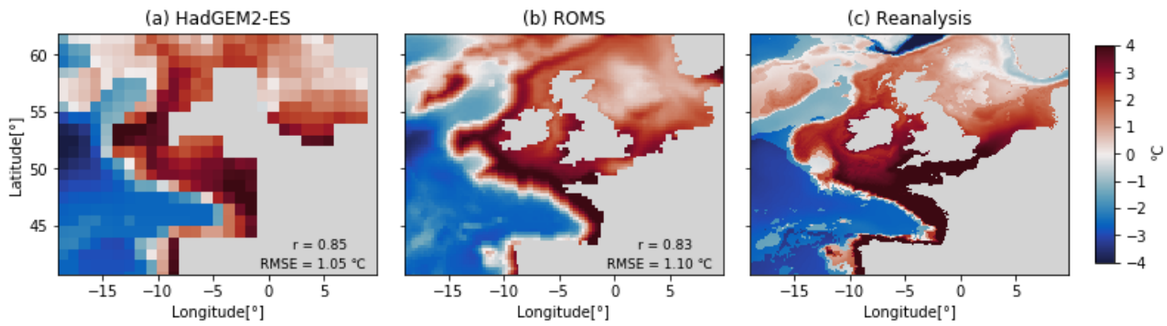

Figure 4.6: The depth averaged temperature anomaly (1993-2012) (w.r.t. the regional mean) of (a) HadGEM2-ES, (b) ROMS and (c) the reanalysis data set.

For the salinity both models simulate low anomalies (w.r.t. the regional mean) on the shelf area and high anomalies in the deeper ocean (Figure 4.7a,b). This is also seen for the reanalysis data (Figure 4.7c), however in the reanalysis there is an inflow of more saline water trough the English Channel compared to the rest of the shelf which is not seen in HadGEM2-ES or ROMS. In the reanalysis relative fresh water (dark blue) is found along the Dutch, Danish, Norwegian and the English coast (mainly in the Irish Sea). In the HadGEM2-ES model half of the North Sea shows relative fresh water. The ROMS simulation shows a large improvement compared to HadGEM2-ES and the relative fresh water is simulated only slightly further into the North Sea compared to the reanalysis data. Also, HadGEM2-ES barely captures the inflow of the Norwegian Trench, in ROMS this is better simulated although the fresher water along the Norwegian coast is underestimated compared to the reanalysis data. The most surprising is the high anomaly between Norway and Denmark in the ROMS simulation, because this is not seen in the HadGEM2-ES simulations and we do not expect a salt water inflow from the Baltic Sea. This may be caused by the combination of the more realistic bathymetry in ROMS allowing more saline water from the deep ocean to enter the Norwegian Trench, but no prescribed Baltic Sea (fresher water) inflow at the boundary. Also the resolution of ROMS, the simulation domain not reaching far enough eastward to capture the Skaggerrak and Kattegat and the interpolation of HadGEM2-ES data eastward on the ROMS grid with a possible different depth can have influenced this. The Norwegian Trench in the reanalysis data has a spatial mean value of -0.35 PSU, both the ROMS and HadGEM2-ES are quite far off with respectively a spatial mean of 0.16 PSU and -0.79 PSU. Overall the spatial correlation is only slightly increased (0.03) in the dynamical downscaled simulation and the RMSE slightly decreased (0.11 PSU). To investigate the performance of the models on the shelf we calculated the spatial correlation and RMSE only for the shelf area. The spatial correlation on the shelf for ROMS is 0.70 (RMSE = 0.33 PSU) and HadGEM2-ES is 0.55 (RMSE = 0.44 PSU). Showing that dynamical downscaling has improved the salinity simulations on the shelf.

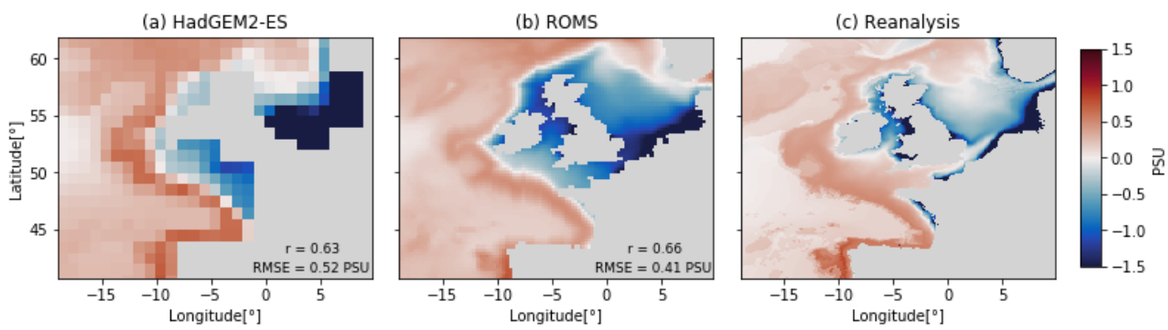

Figure 4.7: The depth averaged salinity anomaly (1993-2012) (w.r.t. the regional mean) of (a) HadGEM2-ES, (b) ROMS and (c) the reanalysis data set.

4.2 Model projections

First we determine the influence of dynamical downscaling with ROMS compared to the HadGEM2-ES simulations for twenty-first century sea-level projections, which gives us information to answer our second research question (Section 4.2.1). Then, we show the HadGEM2-ES and ROMS twenty-first century temperature and salinity projections (Section 4.2.2). Finally, in Section 4.2.3 we investigate the differences between the twenty-first century sea-level projection of the ROMS simulations compared to another set of high resolution simulations with the NEMO model, which allows us to answer our third research question.

4.2.1 Sea-level projections in HadGEM2-ES versus ROMS

The ocean dynamic sea-level change minus IB-effect (ODSLCmIB) over the twenty-first century for HadGEM2-ES and ROMS is computed by taking the difference between the time-mean ODSLCmIB for 1980-2005 and 2074-2098. Both models show an increase in ODSLmIB over the twenty-first century. Over the entire domain the ODSLCmIB spatial mean of HadGEM2-ES (Figure 4.8a) is 4.3 cm higher compared to ROMS (Figure 4.8b). In Figure 4.8c the differences between the ODSLCmIB simulated with ROMS and HadGEM2-ES are shown. On the shelf the ODSLCmIB is locally up to 21 cm smaller in ROMS compared to HadGEM2-ES. This value is found in the north-east of the shelf close to the Norwegian Trench. In the south, the projected changes of HadGEM2-ES are up to 3.4 cm lower compared to ROMS. The differences around Ireland and England may be influenced by the interpolation of the HadGEM2-ES data due to the difference in land mask. We compute a spatial mean (referred to as the coastal spatial mean) over an area spanning from the the Belgian, Dutch and Danish coast, out to the 50 m isobath, and closing in the English Channel at 1° west. This area is of interest, because it is close to high populated areas and expected not to be influenced too much by the deeper ocean. For the ODSLCmIB we find that the coastal spatial mean is 13 cm smaller for ROMS compared to HadGEM2-ES. This value is in the same order of magnitude as found for NEMO compared to HadGEM2-ES in (Hermans, Tinker, et al., 2020), where they found that the ODSLC over the twenty-first century in the North Sea is up to 15.5 cm larger along the southeastern coast for HadGEM2-ES compared to NEMO.

In the local steric SLC the largest changes are seen in the deeper ocean (Figure 4.8d,e), because of the deeper water column (Section 2.1). If the higher SSH in the deep ocean compared to the shelf is not balanced by other forces it will be redistributed and flow onto the shelf (Landerer et al., 2007a) (Figure 4.8g,h). The coastal spatial mean for local steric SLC is 2.8 cm smaller for ROMS compared to HadGEM2-ES (Figure 4.8f), while ROMS projects a 9.9 cm smaller manometric SLC for the coastal spatial mean compared to HadGEM2-ES (Figure 4.8i). So the ROMS coastal spatial mean of 13 cm smaller compared to HadGEM2-ES for the ODSLCmIB is mainly caused by the manometric SLC. The Norwegian Trench is not captured in the bathymetry of HadGEM2-ES, this causes a up to 30 cm higher projection of the ODSLCmIB in the Norwegian Trench compared to ROMS where the Norwegian Trench is captured in the bathymetry. The deeper bathymetry for ROMS in the Norwegian Trench causes higher local steric SLC leading to differences up to 17 cm. The manometric SLC shows differences up to 30 cm lower for ROMS compared to HadGEM2-ES.

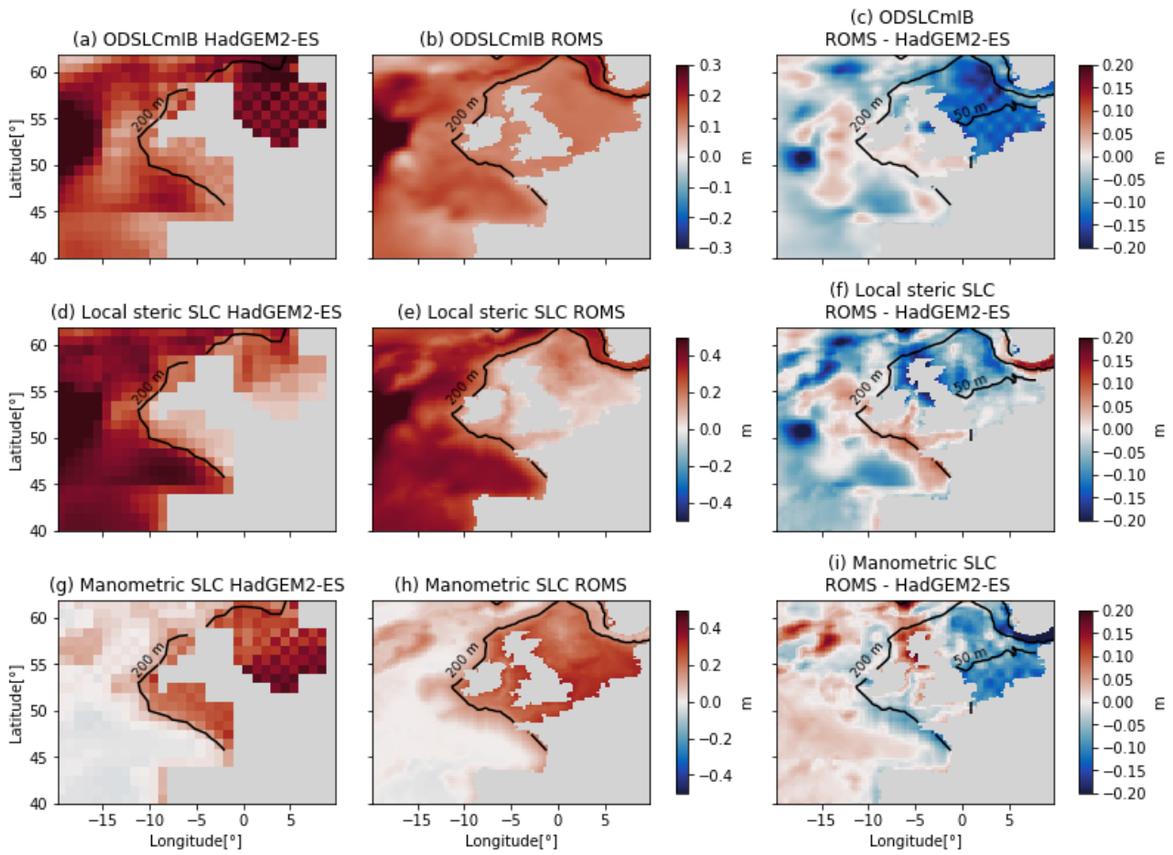

Figure 4.8: The ODSLCmIB, local steric SLC and manomatric SLC (including 'zostoga' (Section 3.3)) between 1980-2005 and 2074-2098 for (a,d,g) HadGEM2-ES, (b,e,h) ROMS and (c,f,i) the difference between ROMS and HadGEM2-ES.

4.2.2 Temperature and Salinity in projections HadGEM2-ES versus ROMS

For the change over the twenty-first century in the depth (weighted) averaged temperature and salinity the time-mean of the period 1980-2005 and 2074-2098 are compared. The change in temperature and salinity cause the local (thermo- and halo-) steric SLC and therefore are interesting to show.

The temperature simulations of both HadGEM2-ES and ROMS (Figure 4.9a,b) project the largest temperature changes on the shelf. The spatial mean changes, in the area deeper than the 200 m isobath (excluding the Norwegian Trench), over the twenty-first century are 1.15 °C (HadGEM2-ES) and 1.01 °C (ROMS) compared to changes up to 4.50 °C on the HadGEM2-ES shelf. The differences between the HadGEM2-ES and ROMS simulation (Figure 4.9c) are relatively small in the deep ocean with a spatial mean of the area outside the 200 m isobath (excluding the Norwegian Trench) of 0.14 °C larger for HadGEM2-ES. The spatial mean on the shelf is 0.40 °C lower in the ROMS simulation. Also the coastal spatial mean of ROMS shows a lower increase temperature of 0.96 °C compared to HadGEM2-ES. The increase of temperature in the Norwegian Trench for ROMS is lower (up to -3.54 °C) in the east and higher (up to 1.31 °C) in the north west compared to HadGEM2-ES.

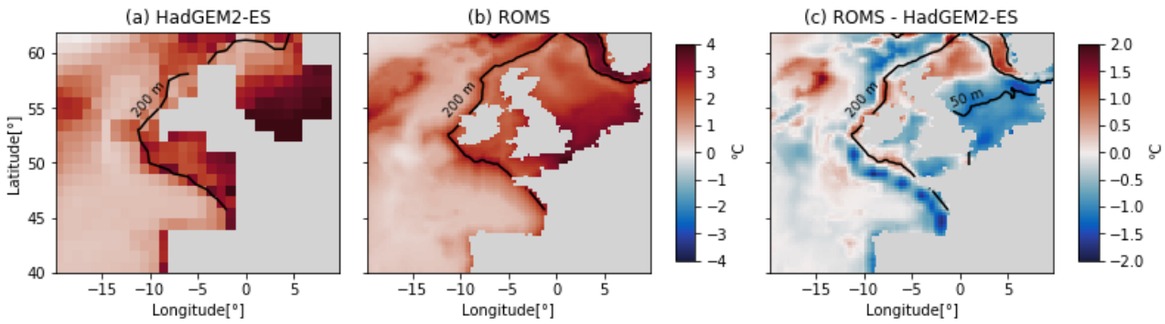

Figure 4.9: The depth averaged temperature change between 1980-2005 and 2074-2098 of (a) HadGEM2-ES, (b) ROMS and (c) the difference between ROMS and HadGEM2-ES.

The changes in salinity in the deep ocean are really small for both models (Figure 4.10a,b). In the area deeper than the 200 m isobath (excluding the Norwegian Trench) the spatial mean of the changes in salinity over the twenty-first century are only -0.097 PSU and -0.036 PSU for respectively HadGEM2-ES and ROMS, compared to changes up to -3.98 PSU on the HadGEM2-ES shelf. The simulations of both models also differ the most on the shelf (Figure 4.10c). There the ROMS simulations are up to 2.23 PSU larger compared to HadGEM2-ES. In the area around England and Ireland ROMS simulates a up to 1.08 PSU higher decay in salinity compared to HadGEM2-ES, however the difference may be partly caused by the interpolation of the HadGEM2-ES data. For the coastal spatial mean area we see the opposite, where ROMS projects a 1.08 PSU lower decay of the salinity for the twenty-first century compared to HadGEM2-ES. In the Norwegian Trench ROMS is up to 3.03 PSU larger compared to HadGEM2-ES, meaning also here the decay in salinity in ROMS is lower than in HadGEM2-ES. We see that ROMS mainly causes a higher salinity in the North Sea, probably due to the opening of the English Channel and the Norwegian Trench being better captured in the bathymetry. Like we saw in the SLC projections also in temperature and salinity simulations the difference in the size of the shelf area of ROMS and HadGEM2-ES is seen.

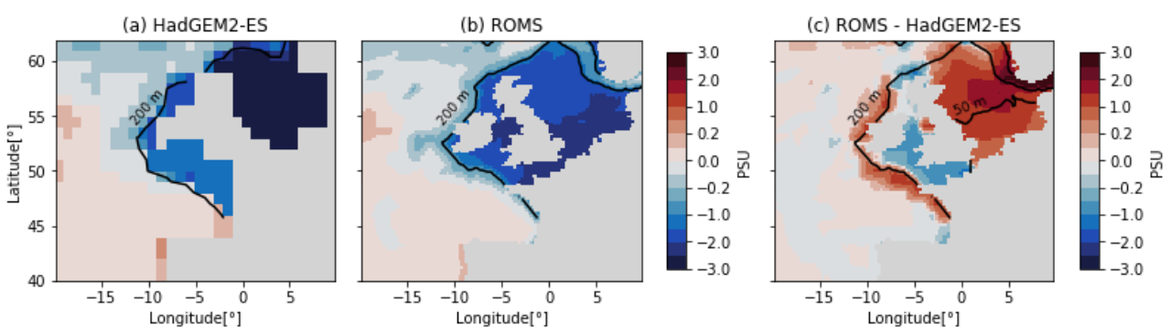

Figure 4.10: The depth averaged salinity change between 1980-2005 and 2074-2098 of (a) HadGEM2-ES, (b) ROMS and (c) the difference between ROMS and HadGEM2-ES. To be able to make both the changes in the deep ocean and on the shelf visible we used a non-linear color scheme.

For both temperature and salinity the largest decrease in density is projected on the shelf, which will cause local steric SLC. However a relative small decrease in density in the deep ocean can still cause a large local steric sea-level rise (Section 2.1). In the deep ocean there is for both HadGEM2-ES and ROMS an increased salinity in the south and decreased salinity in the north, which will cause respectively local halosteric sea-level fall and rise. The temperature increased in the entire domain

for both HadGEM2-ES and ROMS, causing local thermosteric sea-level rise. In the north of the deep ocean the halosteric and thermosteric will amplify each other, while in the south they will compensate each other. In the projections of the local steric SLC (Figure 4.8d,e) we saw a sea-level rise in the full domain. This means that the temperature increase dominates over the salinity increase in the south. In (Hermans, Tinker, et al., 2020) the thermo- and halosteric SLC is calculated for HadGEM2-ES. They found the results we expect from our temperature, salinity and local steric SLC projections: halosteric sea-level rise in the north and halosteric sea-level fall in the south partly compensating the thermosteric sea-level rise over the entire domain. Further does the halo- and thermosteric SLC show how large the local steric SLC is in each part of the domain due to respectively salinity and temperature. This shows that the thermosteric SLC is larger than the halosteric SLC in the deep ocean, while it is the opposite in on the shelf. Hermans, Tinker, et al. (2020) also determined the thermo- and halosteric SLC for NEMO and a similar pattern is seen in the deep ocean, except a small region with thermometric sea-level fall in the north of the deep ocean. Comparing the HadGEM2-ES and NEMO results has shown thermosteric SLC causes a few centimeters difference on the shelf, while halosteric SLC causes changes up to 15 cm on the shelf.

4.2.3 Sea-level projections in NEMO versus ROMS

The ODSLC and ODSLCmIB projections for the twenty-first century for respectively NEMO and ROMS are calculated as the difference between the time-mean for 1980-2005 and respectively 2074-2099 and 2074-2098 (Section 3.4). We assume that the ODSLC (NEMO) and ODSLCmIB (ROMS) over the twenty-first century are comparable (Section 3.4). For both simulations sea-level rise is projected on the shelf (Figure 4.11a,b). A sea-level fall is only seen in the deeper ocean of the NEMO simulations. This also causes the largest difference of 33 cm between ROMS and NEMO (Figure 4.11c). This can be caused by the northern boundary being more northward compared to ROMS, causing it to capture a cold or saline inflow from the north into the domain. Over the entire domain the ROMS simulations are 2.6 cm higher compared to NEMO, largely caused by the sea-level fall in the deep ocean for NEMO. On the shelf, ROMS projects only a 0.1 cm higher sea-level rise compared to NEMO. The simulations for ROMS are slightly higher in the south (up to 5 cm), while the NEMO simulations are slightly higher in the north (up to 5.7 cm). The coastal spatial mean for the ROMS simulation is only 0.77 cm smaller compared to NEMO. It is expected that this difference will be even smaller for lower RCP scenarios, because the projections itself will than be lower.

The largest local steric SLC for NEMO (Figure 4.11d) is found in the deep ocean similar to the ROMS projections (Figure 4.11e). In the NEMO projections of the local steric SLC there is a smaller sea-level rise at the location of the sea-level fall we saw in Figure 4.11a, probably caused by a colder and/or more saline inflow. If we compare the ROMS and NEMO local steric SLC simulations we find that the differences on the shelf are small (Figure 4.11f) with a coastal spatial mean value of 0.23 cm larger for ROMS. South and west around the shelf of ROMS we see larger differences due to a larger area of the NEMO shelf. Here the simulations of ROMS show up to 24 cm larger sea-level rise compared to NEMO. Also in the Norwegian Trench there are large differences. The ROMS simulation is up to 45 cm lower compared to NEMO, which may be caused by a combination of differences in the bathymetry, simulation domain, resolution (in the Norwegian Trench) and the prescribed Baltic Sea inflow at the boundary.

In the manometric SLC there is an opposite pattern compared to the local steric SLC (Figure 4.11g,h). Also for the manometric SLC we see large differences between ROMS and NEMO (Figure 4.11i) outside of the ROMS shelf and inside the Norwegian Trench. Outside of the ROMS shelf the ROMS simulations are up to 17 cm smaller compared to NEMO and the NEMO simulations in the Norwegian Trench can be up to 33 cm smaller compared to ROMS. For the coastal spatial mean the ROMS simulation is only 0.01 cm smaller compared to NEMO.

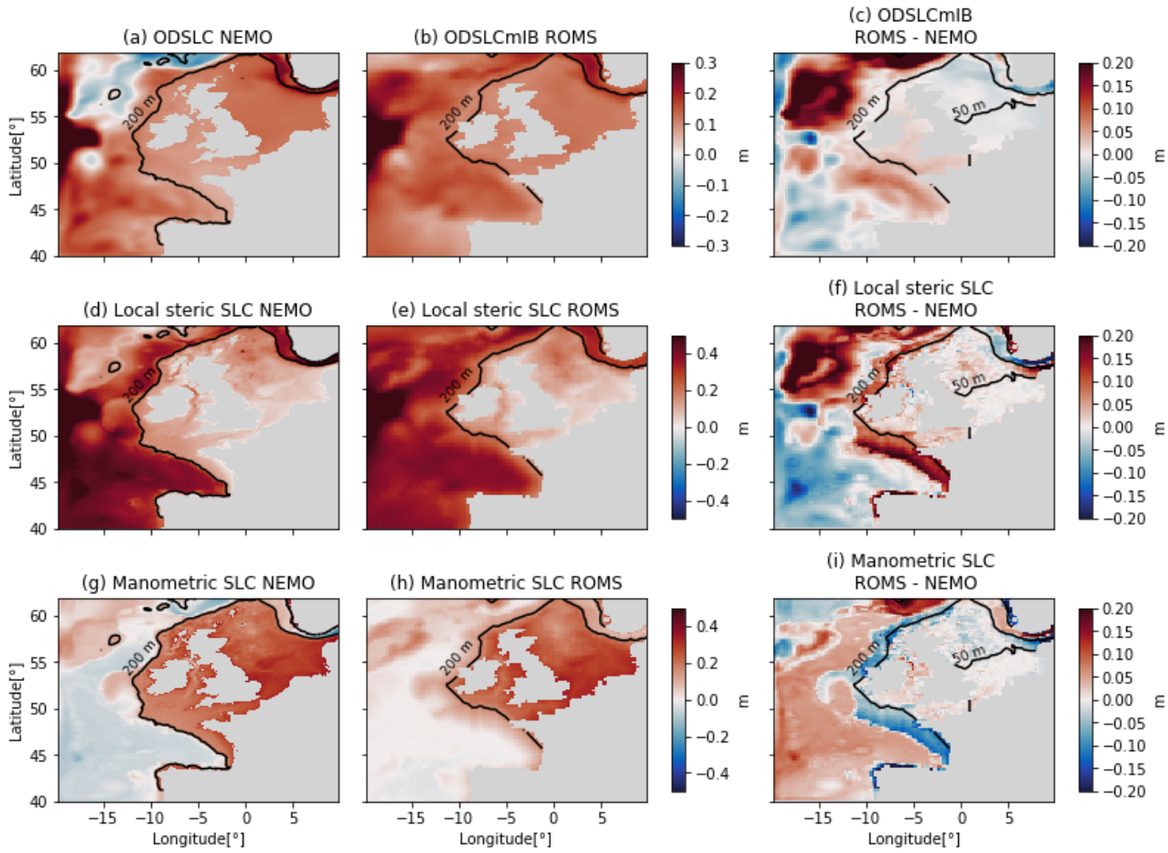

Figure 4.11: The ODLSC(mIB), local steric SLC and manomatric SLC (including 'zostoga' (Section 3.3)) for (a,d,g) NEMO between 1980-2005 and 2074-2099, (b,e,h) ROMS between 1980-2005 and 2074-2098 and (c,f,i) the difference between ROMS and NEMO (assumed that the difference in ODSLC (NEMO) and ODSLCmIB (ROMS) give the difference in ODSLCmIB (Section 3.4)).

Chapter 5

Summary

Research question 1: How do the historical dynamical downscaling simulations with ROMS compare with observations?

In Section 4.1 we have presented the historical simulations of the ROMS model and compared to the observations. Further we have also compared the HadGEM2-ES results to the observations to see the influence of dynamical downscaling. For the MDT we also compared the NEMO results with the observations, to investigate how ROMS compared to the high resolution model. The ROMS simulations for the MDT correlate well with the observations (r=0.89). The relative high increase in spatial correlation for ROMS compared to HadGEM2-ES (0.1) and relative small increase in spatial correlation of NEMO compared to ROMS (0.02), shows that the ROMS simulations might be comparable to NEMO. However the Norwegian coastal current was not well captured in the ROMS simulation. The not prescribed Baltic Sea inflow, the ROMS simulation domain not capturing the Skaggerrak and Kattegat and the lower resolution compared to NEMO (in the Norwegian Trensch) are possible causes.

For the temperature simulations of ROMS and HadGEM2-ES the correlation with the observations where high respectively 0.83 and 0.85. On the shelf ROMS only performed slightly better with a spatial correlation on the shelf of respectively 0.83 and 0.82 for ROMS and HadGEM2-ES. The salinity showed an increase in spatial correlation with the observations for the ROMS simulation (r=0.66) compared to HadGEM2-ES (r=0.63), which was even stronger for the spatial correlation on the shelf with 0.70 and 0.55 for respectively ROMS and HadGEM2-ES. In both the temperature and salinity simulations of ROMS we saw that the area of the Norwegian Trench was not simulated well, with most surprisingly high salinity and temperature anomalies found directly by the entrance of the Baltic Sea. Besides the not prescribed Baltic Sea inflow, the possible to low resolution of ROMS and the domain not reaching far enough eastward to capture the Skaggerrak and Kattegat, also the interpolation of HadGEM2-ES data to the east onto the ROMS grid with possible different depths can have influenced the depth averaged results.

Another part of the validation of the model was the interannual variability of the simulations compared to satellite observations. We found that the variability in the ROMS simulation is relatively high compared to the observations, which is also observed by the HadGEM2-ES model. So ROMS is not able to completely compensate for the to high variability in the HadGEM2-ES model. Finding a time window which clearly fits the observations the best for the entire domain is difficult, because of the difference in timing in internal variability in the climate models and observations (Richter et al., 2017). For the entire domain it is not possible to find a time window which clearly fits the observations. However on the shelf the spatial correlation shows a clear time window for which the ROMS and HadGEM2-ES simulation both correlate the best with the observations. For the time window (1990-2016) where the simulations fit the observations the best, the spatial correlation was the highest for HadGEM2-ES (r=0.79) compared to ROMS (r=0.75), with a respective RMSE of 0.51 and 0.50 for HadGEM2-ES and ROMS. ROMS is expected to solve the processes better in the domain and therefore, especially on the shelf, correlate better with the observations, like we saw for the MDT, temperature and salinity results. There could be different reasons why we did not see the improvement of dynamical downscaling for the interannual variability: the resolution of ROMS can be to low, the satellite data close to the coast can be influenced by land contamination and the smaller shelf of ROMS can have influenced the variability.

Research question 2: Which differences and similarities are seen in the dynamical downscaled sea-level simulations compared to the HadGEM2-ES simulations?

The largest ODSLCmIB differences on the shelf are found in the North Sea, the HadGEM2-ES simulations where up to 21 cm larger compared to ROMS. The ODSLCmIB coastal spatial mean was 13 cm smaller for ROMS than HadGEM2-ES. For the local steric and manometric SLC the coastal spatial mean was respectively 2.8 cm and 9.9 cm smaller for ROMS compared to HadGEM2-ES. This means that close to the Belgium, Dutch and Danish coast the large difference is mainly caused by local steric SLC in the deep ocean or changes outside of the 50 m isobath, that translate into differences in manometric SLC on the shallower parts of the shelf. Also the closed English Channel of the HadGEM2-ES land mask may have influenced the high coastal spatial mean for the manometric

SLC, because the water cannot flow through the channel and spread further over the shelf. Further do we see the differences in the bathymetry back in the projections. Especially the difference in shelf size and and the Norwegian Trench cause large differences.

In the HadGEM2-ES projections of the temperature and salinity we find that the North Sea becomes really warm and fresh compared to ROMS, probably because the coarse grid size causes that the English Channel is closed blocking circulation through the Channel. In ROMS the increase of temperature and decrease of salinity over the twenty-first century are respectively 0.96 °C and 1.08 PSU lower compared to HadGEM2-ES. Further we found small changes in the deep ocean, however because of the large depth of the water column these small changes can still cause relative large steric sea-level change. For both HadGEM2-ES and ROMS we found temperature increase in the entire domain, which will cause local steric sea-level rise. The salinity showed an increase in the south and a decrease in the north, causing respectivaly local steric sea-level fall and rise. In combination with the local steric SLC projections, projecting sea-level rise for the entire domain, we know that the thermosteric sea-level rise in the south is larger than the halosteric sea-level fall.

Research question 3: Which differences and similarities are seen in the dynamical downscaled sea-level simulations with ROMS compared to the previous downscaled simulations using NEMO AMM7?

In the sea-level projections of NEMO and ROMS we see small differences on the shelf. In the coastal area below the 50 m isobath the mean projected ODSLCmIB is only 0.77 cm smaller for ROMS compared to NEMO and the difference is expected to be even smaller for lower RCP scenarios. The largest differences between ROMS and NEMO on the self are 5 cm (higher for ROMS) in the south of the shelf and 5.7 cm (higher for HadGEM2-ES) in the north of the shelf close to the Norwegian Trench. In the south these difference are most likely influenced by the smaller shelf of ROMS. In the Norwegian Trench we also found large differences, which as discussed earlier can be caused by the bathymetry, larger domain, higher resolution (in the Norwegian Trench) and the prescribed Baltic Sea inflow. The differences in the Norwegian Trench for NEMO and ROMS are larger than HadGEM2-ES and ROMS, while the bathymetry is more comparable we assume that the bathymetry is not the main cause. Further do we see a large difference in the north of the deep ocean, however this apparently does not really influence the shelf projections. This fall in the deep ocean for NEMO can be due to the difference in model domain, which makes that it captures a cold or more saline inflow. Further did (Hermans, Tinker, et al., 2020) find a similar themo- and halosteric SLC pattern for NEMO as we expect from the ROMS temperature change, salinity change and local steric SLC simulations.

Chapter 6

Conclusion & Recommendations

We have shown that dynamical downscaling with ROMS mainly improves HadGEM2-ES historical simulations of the MDT and depth averaged salinity on the NWES. For the temperature and interannual sea-level variability the differences between ROMS and HadGEM2-ES where less distinct. For the twenty-first century SLC, depth averaged temperature and salinity change we found large differences between the ROMS and HadGEM2-ES simulations especially in the North Sea. We suppose that dyanmical downscaling with ROMS has improved the HadGEM2-ES projections, because ROMS is expected to better solve the processes on the shelf, has a more realistic bathymetry and land mask and dynamical downscaling with ROMS has improved some of the historical simulations. Compared to NEMO we have shown that ROMS did relatively well for the historical MDT simulations. The increase in spatial correlation with the observations of NEMO compared to ROMS is only small. Also in the projections the simulations compared relatively well on the shelf, especially on the coastal area of Belgium, The Netherlands and Denmark the difference was only 0.77 cm and expected to be even smaller for lower RCP scenarios. This makes the ROMS model more suitable than large scale climate models to be used for projections in the coastal region. However, the small shelf size of ROMS, the Baltic Sea inflow, relative low resolution (in the Norwegian Trench) and possibly the different location of the lateral boundaries compared to NEMO did influence the projections. The shelf representation and the interaction between the Skagerrak and Kattegat cannot be made more realistic using the same grid size, but the Baltic Sea inflow can be improved. The relatively small size of the shelf makes that the ROMS simulations cannot be used close to the edges of the shelf. Therefore adding a more realistic Baltic Sea inflow is advised to determine if this improves the simulations of the ROMS model for the North Sea, specifically for the coastal areas. When the addition of a realistic Baltic Sea inflow not further decreases the difference with the NEMO simulations, we still can conclude that ROMS performs well in the coastal area of Belgium, The Netherlands and Denmark, meaning computational time for dynamically downscaling sea-level projections can be reduced.

To add a Baltic Sea inflow to ROMS, the climatology as used in (Hermans, Tinker, et al., 2020) would be an option. An other option could be calculating the in- and outflow based the salinity changes in the North Sea and the Baltic Sea. For historical simulations observational salinity data of the Baltic Sea can be used, while for simulating projections the salinity data of the Baltic Sea needs to come from salinity projections made of the Baltic Sea. For further analysis of the interannual variability it is suggested to use tide gauge data to find if this compares better to dynamically downscaled simulations than to coarse climate models. Also it would be of interest to investigate the sensitivity of the simulations for the atmospheric forcing. When the atmosphere forcing can be prescribed on a lower frequency, would this lower the computational power. Further is of interest if the sea-level projections are influenced by the RAM used to dynamical downscale the GCM atmosphere component. Furthermore, it is advised to look into the new CMIP6 simulations. Possibly these models can be used to drive downscaling simulations as we did with ROMS. Also ROMS has the option to be used on a higher resolution, which will increase the computational time but might improve the representation of small-scale processes. This would also allow for a comparison of ROMS simulation where only the grid size divers, meaning no internal differences of the ROMs can influence the results. These possible future simulations and analysis can be used to gain further knowledge about the influence of using ROMS on a relative low resolution to dynamical downscale GCM data for which we have found promising results.

Appendix A

Equations ROMS

The ROMS is described by the following equations of motion (Wiki ROMS, 2015):

$$\frac{\partial u}{\partial t} + \vec{v} \cdot \nabla u - fv = -\frac{\partial \phi}{\partial x} - \frac{\partial}{\partial z}(\overline{u'w'} - \nu \frac{\partial u}{\partial z}) + F_u + D_u \tag{A.1}$$

$$\frac{\partial v}{\partial t} + \vec{v} \cdot \nabla v + fu = -\frac{\partial \phi}{\partial y} - \frac{\partial}{\partial z}(\overline{v'w'} - \nu \frac{\partial v}{\partial z}) + F_v + D_v \tag{A.2}$$

where u and v are the horizontal velocities, w is the vertical velocity, f is the Coriolis force, ν is the kinematic viscosity, ψ is the dynamic pressure ($\frac{p}{\rho_0}$), F_u and F_v are the forcing terms and D_u and D_v are the diffusive terms. The primes present the fluctuations around the mean and the overbar represents the time average.

From the equations it can be seen that the Boussinesq approximation and Reynolds averaging are used. The Boussinesq approximation can be made as the density changes in the ocean are small (Cushman-Roisin & Beckers, 2011). Resulting from the Boussinesq approximation the density perturbations can be neglected in the horizontal momentum equations. The vertical momentum equation is reduced to the hydrostatic approximation (Equation A.3). Here the density perturbations cannot be neglected.

$$\frac{\partial \psi}{\partial z} = -\frac{\rho g}{\rho_0} \tag{A.3}$$

further the Boussinesq approximation implies incompressibility of the fluid:

$$\frac{\partial u}{\partial x} + \frac{\partial v}{\partial y} + \frac{\partial w}{\partial z} = 0 \tag{A.4}$$

this means that there is conservation of volume instead of conservation of mass
(Cushman-Roisin & Beckers, 2011).
The following advection-diffusion equation is used to calculate the changes in the scalar concentration field of for example temperature and salinity:

$$\frac{\partial C}{\partial t} + \vec{v} \cdot \nabla C = -\frac{\partial}{\partial z}(\overline{C'w'} - \nu_\theta \frac{\partial C}{\partial z}) + F_c + D_c \tag{A.5}$$

where C can be any scalar field, v_θ is the diffusivity, F_c and D_C are respectively the forcing and diffusive term. The primes present the fluctuations around the mean and the overbar represents the time average.

References

Abram, N., Gattuso, J. P., Prakash, A., Cheng, L., Chidichimo, M. P., Crate, S., Enomoto, H., Garschagen, M., Gruber, N., Harper, S., Holland, E., Kudela, R. M., Rice, J., Steffen, K., & von Schuckmann, K. (2019). *Framing and context of the report. in: Ipcc special report on the ocean and cryosphere in a changing climate.* [Pörtner, H. -O., Roberts, D. C., Masson-Delmotte, V., Zhai, P., Tignor, M., Poloczanska, E., Mintenbeck, K., Alegría, A., Nicolai, M., Okem, A., Petzold, J., Rama, B., Weyer, N. M. (eds.)]. In press. Retrieved from `https://www.ipcc.ch/site/assets/uploads/sites/3/2019/11/05_SROCC_Ch01_FINAL.pdf`

Amante, C., & Eakins, B. W. (2009). *ETOPO1 Global Relief Model converted to PanMap layer format* [data set]. NOAA-National Geophysical Data Center, PANGAEA. doi: 10.1594/PANGAEA.769615

AVIOS+. (2018). *Combined mean dynamic topography - MDT CNES-CLS18* [data set]. Retrieved from `https://www.aviso.altimetry.fr/es/data/products/auxiliary-products/mdt.html` (Accessed at 03-12-2018)

AVISO+. (2018). *Those products were processed by SSALTO/DUACS and distributed by AVISO+ with support from CNES* [data set]. Retrieved from `https://www.aviso.altimetry.fr` (13-02-2018)

Berger, A., & Yin, Q. (2012). Astronomical theory and orbital forcing. In *The sage handbook of environmental change: Volume 1* (pp. 405–425). SAGE Publications Inc. doi: 10.4135/9781446253045.n19

Chapman, D. C. (1985). Numerical Treatment of Cross-Shelf Open Boundaries in a Barotropic Coastal Ocean Model. *Journal of Physical Oceanography*, *15*(8), 1060-1075. doi: 10.1175/1520-0485(1985)015¡1060:NTOCSO¿2.0.CO;2

Church, J. A., Clark, P. U., Cazenave, A., Gregory, J. M., Jevrejeva, S., Levermann, A., Merrifield, M. A., Milne, G. A., Nerem, R. S., Nunn, P. D., Payne, A. J., Pfeffer, W. T., Stammer, D., & Unnikrishnan, A. S. (2013). *Sea level change. Climate Change 2013: The Physical Science Basis. Contribution of Working Group I to the Fifth Assessment Report of the Intergovernmental Panel on Climate Change.* [Stocker, T. F., Qin, D., Plattner G. -K., Tignor, M., Allen, S. K., Boschung, J., Nauels, A., Xia, Y., Bex, V., Midgley P. M. (eds.)]. Cambridge University Press, Cambridge, United Kingdom and New York, NY, USA. Retrieved from `https://www.ipcc.ch/site/assets/uploads/2018/02/WG1AR5_Chapter13_FINAL.pdf`

Collins, M., Knutti, R., Arblaster, J., Dufresne, J. l., Fichefet, T., Friedlingstein, P., Gao, X., Gutowski, W. J., Johns, T., Krinner, G., Shongwe, M., Tebaldi, C., Weaver, A. J., & Wehner, M. (2013). *Long-term Climate Change: Projections, Commitments and Irreversibility. In: Climate Change 2013: The Physical Science Basis. Contribution of Working Group I to the Fifth Assessment Report of the Intergovernmental Panel on Climate Change.* [Stocker, T. F., Qin, D., Plattner G. -K., Tignor, M., Allen, S. K., Boschung, J., Nauels, A., Xia, Y., Bex, V., Midgley P. M. (eds.)]. Cambridge University Press, Cambridge, United Kingdom and New York, NY, USA. Retrieved from `https://www.ipcc.ch/site/assets/uploads/2018/02/WG1AR5_Chapter12_FINAL.pdf`

Cushman-Roisin, B., & Beckers, J.-M. (2011). Boussinesq approximation. In *Introduction to geophysical fluid dynamics* (second ed., p. 828). Elsivier.

Dai, A. (2017). *Dai and Trenberth Global River Flow and Continental Discharge Dataset* [data set]. Boulder CO: Research Data Archive at the National Center for Atmospheric Research, Computational and Information Systems Laboratory. Retrieved from `https://doi.org/10.5065/D6V69H1T`

Dangendorf, S., Calafat, F. M., Arns, A., Wahl, T., Haigh, I. D., & Jensen, J. (2014). Mean sea level variability in the North Sea: Processes and implications. *JGR Oceans*, *119*(10). doi: 10.1002/2014JC009901

Dangendorf, S., Rybski, D., Mudersbach, C., Müller, A., Kaufmann, E., Zorita, E., & Jensen, J. (2014). Evidence for long-term memory in sea level. *Geophysical Research Letters*, *41*(15), 5530–5537. doi: 10.1002/2014GL060538

ENES PORTAL. (2019). *CMIP5 Data Structure.* Retrieved from `https://portal.enes.org/data/enes-model-data/cmip5/datastructure` (Accessed at 14-01-2020)

E.U. Copernicus Marine Service Information. (2020). *ATLANTIC- EUROPEAN NORTH WEST SHELF- OCEAN PHYSICS REANALYSIS* [data set]. Retrieved from

https://resources.marine.copernicus.eu/?option=com_csw&view=details&product_id=NORTHWESTSHELF_REANALYSIS_PHY_004_009 (Accessed at 17-06-2020 (salinity data) and 19-06-2020 (temperature data))

EURO-CORDEX. (2020). *EURO-CORDEX* [data set]. Retrieved from https://www.euro-cordex.net/index.php.en (Accessed at 19-02-2020)

Eyring, V., Bony, S., Meehl, G. A., Senior, C. A., Stevens, B., Stouffer, R. J., , & Taylor, K. E. (2016). Overview of the Coupled Model Intercomparison Project Phase 6 (CMIP6) experimental design and organization. *Geosci. Model Dev.*, *9*, 1937-1958. doi: 10.5194/gmd-9-1937-2016

Fairall, C. W., Bradley, E. F., Rogers, D. P., Edson, J. B., & Young, G. S. (1996). Bulk parameterization of air-sea fluxes for tropical ocean-global atmosphere coupled-ocean atmosphere response experiment. *Journal of Geophysical Research*, *101*(C2), 3747-3764. doi: 10.1029/95JC03205

Fairbanks, R. G. (1989). A 17,OOO-year glacio-eustatic sea level record: influence of glacial melting rates on the Younger Dryas event and deep-ocean circulation. *Nature*, *342*, 637–642. Retrieved from https://www-nature-com.proxy.library.uu.nl/articles/342637a0

Flather, R. A. (1976). A tidal model of the northwest European continental shelf. *Memoires de la Societe Royale de Sciences de Liege*, *6*, 141-164.

Flato, G., Marotzke, J., Abiodun, B., Braconnot, P., Chou, S. C., Collins, W., Cox, P., Driouech, F., Emori, S., Eyring, V., Forest, C., Gleckler, P., Guilyardi, E., Jakob, C., Kattsov, V., Reason, C., & Rummukainen, M. (2013). *Evaluation of climate models. in: Climate change 2013: The physical science basis. contribution of working group i to the fifth assessment report of the intergovernmental panel on climate change.* [Stocker, T. F., Qin, D., Plattner G. -K., Tignor, M., Allen, S. K., Boschung, J., Nauels, A., Xia, Y., Bex, V., Midgley P. M. (eds.)]. Cambridge University Press, Cambridge, United Kingdom and New York, NY, USA. Retrieved from https://www.ipcc.ch/site/assets/uploads/2018/02/WG1AR5_Chapter09_FINAL.pdf

Frederikse, T., & Gerkema, T. (2018). Multi-decadal variability in seasonal mean sea level along the North Sea coast. *Ocean Science*, *14*(6), 1491–1501. doi: 10.5194/os-14-1491-2018

Frederikse, T., Riva, R., Kleinherenbrink, M., Wada, Y., Marzeion, B., & Van den Broeke, M. (2016). Closing the sea level budget on a regional scale: Trends and variability on the northwestern european continental shelf. *Geophysical Research Letters*, *43*. doi: 10.1002/2016GL070750

Gerkema, T., & Duran-Matute, M. (2017). Interannual variability of mean sea level and its sensitivity to wind climate in an inter-tidal basin. *Earth System Dynamics*, *8*, 1223-1235. doi: 10.5194/esd-8-1223-2017

Goosse, H. (2015). Brief History of Climate: Causes and Mechanisms. In *Climate systems dynamics and modelling* (first ed.). New York: Cambrige University press. Retrieved from https://assets.cambridge.org/97811070/83899/frontmatter/9781107083899_frontmatter.pdf

Greatbatch, R. J. (1994). A note on the representation of steric sea level in models that conserve volume rather than mass. *JGR Oceans*, *99*(C6), 12767-12771. doi: 10.1029/94JC00847

Gregory, J., Griffies, S., Hughes, C., Lowe, J., Church, J., Fukimori, I., Gomez, N., Kopp, R., Landerer, F., Le Cozannet, G., Ponte, R., Stammer, D., Tamisiea, M., & van de Wal, R. (2019). Concepts and terminology for sea level: Mean, variability and change, both local and global. doi: 10.1007/s10712-019-09525-z

Griffies, S. M., & Greatbatch, R. J. (2012). Physical processes that impact the evolution of global mean sea level in ocean climate models. *Ocean Modelling*, *51*, 37–72. doi: 10.1016/j.ocemod.2012.04.003

Hartmann, D., Klein Tank, A. M. G., Rusticucci, M., Alexander, L. V., Brönnimann, S., Charabi, Y., Dentener, F. J., Dlugokencky, E. J., Easterling, D. R., Kaplan, A., Soden, B. J., Thorne, P. W., Wild, M., & Zhai, P. M. (2013). *Observations: Atmosphere and Surface. In: Climate Change 2013: The Physical Science Basis. Contribution of Working Group I to the Fifth Assessment Report of the Intergovernmental Panel on Climate Change.* [Stocker, T. F., Qin, D., Plattner G. -K., Tignor, M., Allen, S. K., Boschung, J., Nauels, A., Xia, Y., Bex, V., Midgley P. M. (eds.)]. Cambridge University Press, Cambridge, United Kingdom and New York, NY, USA. Retrieved from https://www.ipcc.ch/site/assets/uploads/2017/09/WG1AR5_Chapter02_FINAL.pdf

Hawkins, E., & Sutton, R. (2012). Time of emergence of climate signals. *Geophysical Research Letters*, *39*(1). doi: 10.1029/2011GL050087

Hermans, T. H. J., Le Bars, D., Katsman, C. A., Camargo, C. M. L., Gerkema, T., Calafat, F. M., Tinker, J., & Slangen, A. B. A. (2020). Drivers of interannual sea level variability on the northwestern european shelf. *JGR Oceans*, *125*(10). doi: 10.1029/2020JC016325

Hermans, T. H. J., Tinker, J., Palmer, M. D., Katsman, C. A., Vermeersen, B. L. A., & Slangen, A. B. A. (2020). Improving sea-level projections on the Northwestern European shelf using dynamical downscaling. *Climate Dynamics*, *54*, 1987–2011. doi: 10.1007/s00382-019-05104-5

Hock, R., Rasul, G., Adler, C., Cáceres, B., Gruber, S., Hirabayashi, Y., Jackson, M., Kääb, A., Kang, S., Kutuzov, S., Milner, A., Molau, U., Morin, S., Orlove, B., & Steltzer, H. (2019). *High*

Mountain Areas. In: IPCC Special Report on the Ocean and Cryosphere in a Changing Climate. [Pörtner, H. -O., Roberts, D. C., Masson-Delmotte, V., Zhai, P., Tignor, M., Poloczanska, E., Mintenbeck, K., Alegría, A., Nicolai, M., Okem, A., Petzold, J., Rama, B., Weyer, N. M. (eds.)]. In press. Retrieved from https://www.ipcc.ch/site/assets/uploads/sites/3/2019/11/06_SROCC_Ch02_FINAL.pdf

Hurrell, J. W. (1995). Decadal trends in the north atlantic oscillation: Regional temperatures and precipitation. *Science*, *269*(5224), 676–679. Retrieved from http://www.jstor.org/stable/2888966

Huthnance, J. M. (1984). Slope Currents and "JEBAR". *Journal of Physical Oceanography*, *14*(4), 795–810. doi: 10.1175/1520-0485(1984)014¡0795:SCA¿2.0.CO;2

Jevrejeva, S., Moore, J., Woodworth, P., & Grinsted, A. (2005). Influence of large-scale atmospheric circulation on European sea level: results based on the wavelet transform method. *Tellus A: Dynamic Meteorology and Oceanography*, *57*(2), 183–193. doi: 10.3402/tellusa.v57i2.14609

Jones, P. D., Jonsson, T., & Wheeler, D. A. (1997). *Monthly values of the North Atlantic Oscillation Index from 1821 to 2000* [data set]. PANGAEA. doi: 10.1594/PANGAEA.56559

Knutti, R., Abramowitz, G., Collins, M., Eyring, V., Gleckler, P. J., Hewitson, B., & Mearns, L. (2010). *Good Practice Guidance Paper on Assessing and Combining Multi Model Climate Projections. In: Meeting Report of the Intergovernmental Panel on Climate Change Expert Meeting on Assessing and Combining Multi Model Climate Projections.* [Stocker, T.F., Qin, D., Plattner, G. -K.,Tignor, M., Midgley, P.M. (eds.)]. IPCC Working Group I Technical Support Unit, University of Bern, Bern, Switzerland. Retrieved from https://wg1.ipcc.ch/docs/IPCC_EM_MME_GoodPracticeGuidancePaper.pdf

Kristiansen, T. (2020). *model2roms.* Retrieved from https://github.com/trondkr/model2roms (Accessed at 11-03-2020)

Landerer, F. W., Jungclaus, J. H., & Marotzke, J. (2007a). Ocean bottom pressure changes lead to a decreasing length-of-day in a warming climate. *Geophysical Research Letters*, *34*(6). doi: 10.1029/2006GL029106

Landerer, F. W., Jungclaus, J. H., & Marotzke, J. (2007b). Regional Dynamic and Steric Sea Level Change in Response to the IPCC-A1B Scenario. *Journal of Physical Oceanography*, *37*(2), 296–312. Retrieved from https://doi.org/10.1175/JPO3013.1 doi: 10.1175/JPO3013.1

Li, J., Tan, W., Chen, M., Zuo, J., & Yang, Y. (2016). The regional patterns of the global dynamic and steric sea level variation in twenty-first century projections. *Global and Planetary Change*, *146*, 133–139. doi: 10.1016/j.gloplacha.2016.10.005

Liu, Z. J., Minobe, S., Sasaki, Y. N., & Terada, M. (2016). Dynamical downscaling of future sea level change in the western North Pacific using ROMS. *Journal of Oceanography*, *72*(6), 905–922. doi: 10.1007/s10872-016-0390-0

Lyu, K., Zhang, X., Church, J. A., Slangen, A. B. A., & Hu, J. (2014). Time of emergence for regional sea-level change. *Nature Climate Change*, *4*(11), 1006–1010. doi: 10.1038/nclimate2397

Madec, G., & the NEMO team. (2016). NEMO ocean engine.

Marchesiello, P., McWilliams, J. C., & Shchepetkin, A. (2001). Open boundary conditions for long-term integration of regional ocean models. *Ocean Modelling*, *3*, 1-20. Retrieved from https://marine.rutgers.edu/po/Papers/obc_oc.pdf

Mathis, M., Mayer, B., & Pohlmann, T. (2013). An uncoupled dynamical downscaling for the North Sea: Method and evaluation. *Ocean Modelling*, *72*, 153–166. doi: 10.1016/j.ocemod.2013.09.004

Melet, A., & Meyssignac, B. (2015). Explaining the Spread in Global Mean Thermosteric Sea Level Rise in CMIP5 Climate Models*. , *28*(24), 9918–9940. doi: 10.1175/JCLI-D-15-0200.1

Met Office. (2020). *HadGEM2 family: Met Office climate prediction model.* Retrieved from https://www.metoffice.gov.uk/research/approach/modelling-systems/unified-model/climate-models/hadgem2 (Accessed at 04-08-2020)

Muller, R., & MacDonald, G. (1997). Glacial Cycles and Astronomical Forcing. *Science*, *277*(5323). Retrieved from https://www.jstor.org/stable/2893568

O'Neill, B. C., Tebaldi, C., Van Vuuren, D. P., Eyring, V., Friedlingstein, P., Hurtt, G., Knutti, R., Kriegler, E., Lamarque, J. F., Lowe, J., Meehl, G. A., Moss, R., Riahi, K., & Sanderson, B. M. (2016). The Scenario Model Intercomparison Project (ScenarioMIP) for CMIP6. *Geoscientific Model Development*, *9*(9), 3461–3482. doi: 10.5194/gmd-9-3461-2016

Oppenheimer, M., Glavovic, B. C., Hinkel, J., van de Wal, R., Magnan, A. K., Abd-Elgawad, A., Cai, R., Cifuentes-Jara, M., DeConto, R. M., Ghosh, T., Hay, J., Isla, F., Marzeion, B., Meyssignac, B., & Sebesvari, Z. (2019). *Sea Level Rise and Implications for Low-Lying Islands, Coasts and Communities. In: IPCC Special Report on the Ocean and Cryosphere in a Changing Climate.* [Pörtner, H. -O., Roberts, D. C., Masson-Delmotte, V., Zhai, P., Tignor, M., Poloczanska, E.,

Mintenbeck, K., Alegría, A., Nicolai, M., Okem, A., Petzold, J., Rama, B., Weyer, N. M. (eds.)]. In press. Retrieved from https://www.ipcc.ch/site/assets/uploads/sites/3/2019/11/08_SROCC_Ch04_FINAL.pdf

Orlanski, I. (1976). A simple boundary condition for unbounded hyperbolic flows. *Journal of Computational Physics*, *21*(3), 251-269. doi: 10.1016/0021-9991(76)90023-1

Papadopoulos, A., & Tsimplis, M. N. (2006). Coherent Coastal Sea-Level Variability at Interdecadal and Interannual Scales from Tide Gauges. *Journal of Coastal Research*, *2006*(223), 625–639. doi: 10.2112/04-0156.1

Quante, M., Colijn, F., Bakker, J. P., Härdtle, W., Heinrich, H., Lefebvre, C., Nöhren, I., Olesen, J. E., Pohlmann, T., Sterr, H., Sündermann, J., & Tölle, M. H. (2016). Introduction to the assessment—characteristics of the region. In M. Quante & F. Colijn (Eds.), *North sea region climate change assessment* (pp. 1–52). Cham: Springer International Publishing. doi: 10.1007/978-3-319-39745-0_1

Rhein, M., Rintoul, S. R., Aoki, S., Campos, E., Chambers, D., Feely, R. A., Gulev, S., Johnson, G. C., Josey, S. A., Kostianoy, A., Mauritzen, C., Roemmich, D., Talley, L. D., & Wang, F. (2013). *Observations: Ocean. In: Climate Change 2013: The Physical Science Basis. Contribution of Working Group I to the Fifth Assessment Report of the Intergovernmental Panel on Climate Change* . [Stocker, T. F., Qin, D., Plattner G. -K., Tignor, M., Allen, S. K., Boschung, J., Nauels, A., Xia, Y., Bex, V., Midgley P. M. (eds.)]. Cambridge University Press, Cambridge, United Kingdom and New York, NY, USA. Retrieved from https://www.ipcc.ch/site/assets/uploads/2018/02/WG1AR5_Chapter03_FINAL.pdf

Richter, K., Øie Nilsen, J. E., Raj, R. P., Bethke, I., Johannessen, J. A., Slangen, A. B. A., & Marzeion, B. (2017). Northern North Atlantic Sea Level in CMIP5 Climate Models: Evaluation of Mean State, Variability, and Trends against Altimetric Observations. *Journal of Climate*, *30*(23), 9383-9398. doi: 10.1175/JCLI-D-17-0310.1

Ricker, M., & Stanev, E. V. (2020). Circulation of the european northwest shelf: a lagrangian perspective. *Ocean Science*, *16*(3), 637–655. doi: 10.5194/os-16-637-2020

Rio, M. H., Mulet, S., & Picot, N. (2014). Beyond GOCE for the ocean circulation estimate: Synergetic use of altimetry, gravimetry, and in situ data provides new insight into geostrophic and Ekman currents. *Geophysical Research Letters*, *41*(24), 8918–8925. doi: 10.1002/2014GL061773

Rogers, J. C. (1984). The Association between the North Atlantic Oscillation and the Southern Oscillation in the Northern Hemisphere. *Monthly Weather Review*, *112*(10), 1999-2015. doi: 10.1175/1520-0493(1984)112¡1999:TABTNA¿2.0.CO;2

Rossby Centre. (2020). *Rossby Centre regional atmospheric model, RCA4.* Retrieved from https://www.smhi.se/en/research/research-departments/climate-research-rossby-centre2-552/rossby-centre-regional-atmospheric-model-rca4-1.16562

Stahl, K., Weiler, M., Kohn, I., Freudiger, D., Seibert, J., Vis, M., Gerlinger, K., & Böhm, M. (2016). *The snow and glacier melt components of streamflow of the river Rhine and its tributaries considering the influence of climate change - Synthesis report.* International Commission for the Hydrology of the Rhine Basin (KHR/CHR). Retrieved from https://www.ipcc.ch/site/assets/uploads/2018/02/WG1AR5_Chapter12_FINAL.pdf

Stammer, D., & Hüttemann, S. (2008). Response of regional sea level to atmospheric pressure loading in a climate change scenario. *Journal of Climate*, *21*(10), 2093–2101. doi: 10.1175/2007JCLI1803.1

Sterlini, P., Le Bars, D., de Vries, H., & Ridder, N. (2017). Understanding the spatial variation of sea level rise in the North Sea using satellite altimetry. *Journal of Geophysical Research: Oceans*, *122*(8), 6498–6511. doi: 10.1002/2017JC012907

Taylor, K. E., Stouffer, R. J., & Meehl, G. A. (2012). An Overview of CMIP5 and the Experiment Design. *Bulletin of the American Meteorological Society*, *93*(4), 485-498. doi: 10.1175/BAMS-D-11-00094.1

Tsimplis, M. N., Woolf, D. K., Osborn, T. J., Wakelin, S., Wolf, J., Flather, R., Shaw, A. G., Woodworth, P., Challenor, P., Blackman, D., Pert, F., Yan, Z., & Jevrejeva, S. (2005). Towards a vulnerability assessment of the UK and northern European coasts: The role of regional climate variability. *Philosophical Transactions of the Royal Society A: Mathematical, Physical and Engineering Sciences*, *363*(1831), 1329–1358. doi: 10.1098/rsta.2005.1571

van de Wal, R. S. W., Zhang, X., Minobe, S., Jevrejeva, S., Riva, R. E. M., Little, C., Richter, K., & Palmer, M. D. (2019). Uncertainties in Long-Term Twenty-First Century Process-Based Coastal Sea-Level Projections. *Surveys in Geophysics*, *40*(6), 1655–1671. doi: 10.1007/s10712-019-09575-3

van Vuuren, D. P., Edmonds, J., Kainuma, M., Riahi, K., Thomson, A., Hibbard, K., Hurtt, G. C., Kram, T., Krey, V., Lamarque, J. F., Masui, T., Meinshausen, M., Nakicenovic, N., Smith, S. J., & Rose, S. K. (2011). The representative concentration pathways: An overview. *Climatic Change*, *109*(1), 5–31. doi: 10.1007/s10584-011-0148-z

Vermeersen, B. L., Slangen, A. B., Gerkema, T., Baart, F., Cohen, K. M., Dangendorf, S., Duran-Matute, M., Frederikse, T., Grinsted, A., Hijma, M. P., Jevrejeva, S., Kiden, P., Kleinherenbrink, M., Meijles, E. W., Palmer, M. D., Rietbroek, R., Riva, R. E., Schulz, E., Slobbe, D. C., Simpson, M. J., Sterlini, P., Stocchi, P., Van De Wal, R. S., & Van Der Wegen, M. (2018). Sea-level change in the Dutch Wadden Sea. *Netherlands Journal of Geosciences*, *97*(3), 79–127. doi: 10.1017/njg.2018.7

Wahl, T., Haigh, I., Woodworth, P., Albrecht, F., Dillingh, D., Jensen, J., Nicholls, R., Weisse, R., & Wöppelmann, G. (2013). Observed mean sea level changes around the north sea coastline from 1800 to present. *Earth-Science Reviews*, *124*, 51 - 67. doi: https://doi.org/10.1016/j.earscirev.2013.05.003

Wakelin, S. L., Woodworth, P. L., Flather, R. A., & Williams, J. A. (2003). Sea-level dependence on the NAO over the NW European continental shelf. *Geophysical Research Letters*, *30*(7). doi: 10.1029/2003GL017041

Wiki ROMS. (2015). *Equations of motion.* Retrieved from `https://www.myroms.org/wiki/Equations_of_Motion` (Accessed at 15-01-2020)

Wiki ROMS. (2020). *cppdefs.h.* Retrieved from `https://www.myroms.org/wiki/cppdefs.h` (Accessed at 05-08-2020)

Winther, N., & Johannessen, J. (2006). North sea circulation: Atlantic inflow and its destination. *Journal of Geophysical Research Oceans*, *111*(C12). doi: 10.1029/2005JC003310

Yin, J., Griffies, S. M., & Stouffer, R. J. (2010). Spatial variability of sea level rise in twenty-first century projections. *Journal of Climate*, *23*(17), 4585–4607. doi: 10.1175/2010JCLI3533.1

Zhang, X., Church, J. A., Monselesan, D., & McInnes, K. L. (2017). Sea level projections for the Australian region in the 21st century. *Geophysical Research Letters*, *44*(16), 8481–8491. doi: 10.1002/2017GL074176